

# Prospects for Spin-1 Resonance Search at 13 TeV LHC and the ATLAS Diboson Excess

Tomohiro Abe<sup>(a)</sup>, Teppei Kitahara<sup>(a)</sup>, and Mihoko M. Nojiri<sup>(a,b,c)</sup>

<sup>(a)</sup>*KEK Theory Center, IPNS, KEK, Tsukuba, Ibaraki 305-0801, Japan*

<sup>(b)</sup>*The Graduate University of Advanced Studies (Sokendai),  
Tsukuba, Ibaraki 305-0801, Japan*

<sup>(c)</sup>*Kavli IPMU (WPI), University of Tokyo, Kashiwa, Chiba 277-8583, Japan*

## Abstract

Motivated by ATLAS diboson excess around 2 TeV, we investigate a phenomenology of spin-1 resonances in a model where electroweak sector in the SM is weakly coupled to strong dynamics. The spin-1 resonances,  $W'$  and  $Z'$ , are introduced as effective degrees of freedom of the dynamical sector. We explore several theoretical constraints by investigating the scalar potential of the model as well as the current bounds from the LHC and precision measurements. It is found that the main decay modes are  $V' \rightarrow VV$  and  $V' \rightarrow Vh$ , and the  $V'$  width is narrow enough so that the ATLAS diboson excess can be explained. In order to investigate future prospects, we also perform collider simulations at  $\sqrt{s} = 13$  TeV LHC, and obtain a model independent expected exclusion limit for  $\sigma(pp \rightarrow W' \rightarrow WZ \rightarrow JJ)$ . We find a parameter space where the diboson excess can be explained, and are within a reach of the LHC at  $\int dt \mathcal{L} = 10 \text{ fb}^{-1}$  and  $\sqrt{s} = 13$  TeV.

---

*E-mail:* [abetomo@post.kek.jp](mailto:abetomo@post.kek.jp)

*E-mail:* [kteppei@post.kek.jp](mailto:kteppei@post.kek.jp)

*E-mail:* [nojiri@post.kek.jp](mailto:nojiri@post.kek.jp)

---

# Contents

<b>1</b>	<b>Introduction</b>	<b>1</b>
<b>2</b>	<b>The partially composite standard model</b>	<b>3</b>
2.1	The model setup . . . . .	3
2.2	Model parameters . . . . .	8
<b>3</b>	<b>Phenomenology of spin-1 resonances</b>	<b>8</b>
3.1	Properties of the extra vector bosons . . . . .	9
3.2	Constraints on the model . . . . .	13
3.2.1	Theoretical constraints . . . . .	13
3.2.2	Experimental constraints . . . . .	15
3.2.3	Summary of the constraints . . . . .	16
3.3	Current status: 8 TeV analyses . . . . .	19
<b>4</b>	<b>MC simulation of <math>W' \rightarrow WZ</math> at <math>\sqrt{s} = 13</math> TeV</b>	<b>23</b>
<b>5</b>	<b>Future prospects: 13 TeV analyses</b>	<b>26</b>
<b>6</b>	<b>Conclusion</b>	<b>29</b>
<b>A</b>	<b>Viable range of the coupling ratio <math>\kappa_Z</math></b>	<b>31</b>
<b>B</b>	<b>Production cross sections of <math>W'</math> and <math>Z'</math></b>	<b>33</b>
<b>C</b>	<b>Renormalization group equations</b>	<b>33</b>

---

## 1 Introduction

The ATLAS experiment recently reported an excess of the events in the search for the diboson resonance, in the  $pp \rightarrow (WW, WZ, \text{ and } ZZ) \rightarrow JJ$  channels, where  $J$  is a fat-jet formed by boosted  $W$  or  $Z$  boson [1]. The largest local significance is  $3.4 \sigma$  around 2 TeV in the  $WZ$  channel, and the global significance is  $2.5 \sigma$ . The CMS experiment also studied the same channels. The largest deviation they found is  $1.4 \sigma$  at  $\sim 1.9$  TeV [2]. Although we cannot conclude that there is a new particle with the mass around 2 TeV from this data, it is worthwhile to consider models which can explain this excess, and many papers have already appeared discussing interpretations of the excess [3–18]. As discussed in these references, a simple candidate is a spin-1 particle.

New vector resonances often appear in the models with dynamical symmetry breaking. Such spin-1 resonances appear in the composite Higgs scenario [19–22] with the dynamics at TeV scale to account for the naturalness problem. Since the models are based on the non-Linear sigma models, the effective theory involves many operators whose coefficients are unknown. They possibly affect to the couplings of the new spin-1 particles to the standard model (SM) particles, and thus there is uncertainty in the prediction of the  $W'$  couplings.

Another way to include spin-1 particles is to extend the electroweak gauge symmetry. We can easily introduce new spin-1 particles in renormalizable manner. In that case, the models are calculable and we can avoid the operators whose coefficients are unknown, in contrast to the models based on the non-linear sigma models. Besides, some renormalizable models with extended gauge sector can be regarded as the low energy effective theory of UV theory with some dynamics.

Such renormalizable models have been discussed in the context of the left-right (LR) symmetric model [8, 17, 18] and the leptophobic G221 model [11]. These models contain the right-handed SM fermions which are not singlet under the new gauge symmetry. In such case, the couplings of the SM fermions to the new gauge boson are not suppressed, and the new gauge bosons mainly decay into the SM fermions.

It is also possible to use linear sigma model, instead of non-linear sigma models, for models emerged from the dynamics at TeV scale. An example was proposed in Ref. [23]. This model, called the partially composite standard model, has three Higgs fields. Two of them are regarded as effective degrees of freedom below the dynamical scale. The other one is an elementary field. Spin-1 resonances are introduced as new gauge bosons *a la* Hidden local symmetry [24–27]. A feature of the model is that the SM fermion are singlet under the new gauge symmetry, and thus all the fermion couplings to the new gauge bosons are suppressed by the mixing angle in the gauge sector. As a result, the new gauge bosons mainly decay into the SM gauge bosons. This is an important feature of this model.

In this paper, we investigate the possibility to explain the diboson excess by the partially composite standard model, and also the future prospects of  $W'$  and  $Z'$  bosons searches at the LHC Run-2, where  $\sqrt{s} = 13$  TeV. We perform a comprehensive study to find the parameter space which has not been excluded from current experimental data. The constraints on the model parameters come from the LHC searches and the electroweak precision measurements. We also require theoretical constraints such as perturbativity condition, bounded below condition, global minimum vacuum condition, and stability condition of the scalar potential. We find a parameter space where the diboson excess can be explained.

We further investigate a model-independent sensitivity at the LHC Run-2 by generating both signal  $pp \rightarrow W' \rightarrow WZ$  and dijet background events, and performing detector simulations.

We organize the rest of this paper as follows. We briefly review the partially composite standard model in Sec. 2. In Sec. 3, we show the constraints to the model, and find

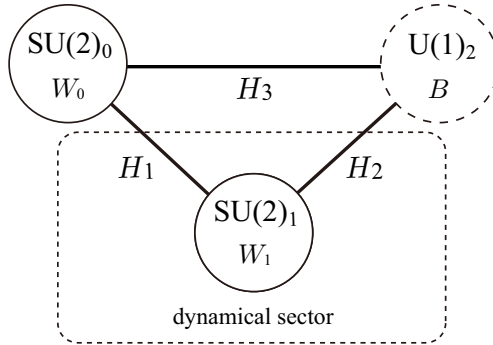


Figure 1. The moose diagram of this setup: the circles represent the gauge groups, and the thick lines that connect two circles are the Higgs fields. The Higgs fields  $H_1$ ,  $H_2$ , and  $SU(2)_1$  gauge group can be regarded as the operators originated from the dynamical sector.

that there are parameter regions where are consistent with the ATLAS excess. In Sec. 4, we perform the collider simulations for the signal and the background, and obtain the sensitivity at the LHC Run-2. In Sec. 5, we investigate the future prospects of the spin-1 resonances search using our simulation results. Section 6 is devoted for conclusion.

## 2 The partially composite standard model

### 2.1 The model setup

In the partially composite standard model, the gauge symmetry of the electroweak sector is  $SU(2)_0 \times SU(2)_1 \times U(1)_2$ , and three Higgs fields ( $H_1$ ,  $H_2$ ,  $H_3$ ) are introduced for the symmetry breaking,  $SU(2)_0 \times SU(2)_1 \times U(1)_2 \rightarrow U(1)_{EM}$ . We denote the gauge couplings  $g_0$ ,  $g_1$ , and  $g_2$ , respectively. The three gauge couplings are related to the QED coupling as

$$\frac{1}{e^2} = \frac{1}{g_0^2} + \frac{1}{g_1^2} + \frac{1}{g_2^2}. \quad (1)$$

Here, we assume that the  $SU(2)_1$  gauge symmetry belongs to a dynamical sector, and  $g_1 \gg g_0, g_2$ . Under this assumption,  $g_0$  and  $g_2$  are approximately  $g_W$  and  $g_Y$  which are the gauge couplings of  $SU(2)_L$  and  $U(1)_Y$ , respectively. We regard the gauge field associated with  $SU(2)_1$  as the vector resonance originated from unknown dynamics above TeV scale. This implies that fields transformed under the  $SU(2)_1$  gauge symmetry also belong to the dynamical sector. We take  $H_1$  and  $H_2$  as such fields, and regard  $H_3$  as an elementary field. All the fermions are also elementary, and they are singlet under  $SU(2)_1$ . We schematically show the model structure in the moose notation [28] in Fig. 1, and also summarize the field contents and their charge assignments in Table 1.



Table 1. The charge assignment of the partially composite standard model. Only  $H_1$  and  $H_2$  are the representations of the  $SU(2)_1$  gauge symmetry.

Fields	$SU(2)_0$	$U(1)_2$	$SU(3)_c$	$SU(2)_1$
$H_1$	<b>2</b>	0	<b>1</b>	<b>2</b>
$H_2$	<b>1</b>	1/2	<b>1</b>	<b>2</b>
$H_3$	<b>2</b>	1/2	<b>1</b>	<b>1</b>
$Q$	<b>2</b>	1/6	<b>3</b>	<b>1</b>
$u_R$	<b>1</b>	2/3	<b>3</b>	<b>1</b>
$d_R$	<b>1</b>	-1/3	<b>3</b>	<b>1</b>
$L$	<b>2</b>	-1/2	<b>1</b>	<b>1</b>
$e_R$	<b>1</b>	-1	<b>1</b>	<b>1</b>

The scalar potential is given as<sup>#1</sup>

$$\begin{aligned}
V(H_1, H_2, H_3) = & \mu_1^2 \text{tr}(H_1 H_1^\dagger) + \mu_2^2 \text{tr}(H_2 H_2^\dagger) + \mu_3^2 \text{tr}(H_3 H_3^\dagger) \\
& + \kappa \text{tr}(H_1 H_2 H_3^\dagger) \\
& + \lambda_1 (\text{tr}(H_1 H_1^\dagger))^2 + \lambda_2 (\text{tr}(H_2 H_2^\dagger))^2 + \lambda_3 (\text{tr}(H_3 H_3^\dagger))^2 \\
& + \lambda_{12} \text{tr}(H_1 H_1^\dagger) \text{tr}(H_2 H_2^\dagger) + \lambda_{23} \text{tr}(H_2 H_2^\dagger) \text{tr}(H_3 H_3^\dagger) \\
& + \lambda_{31} \text{tr}(H_3 H_3^\dagger) \text{tr}(H_1 H_1^\dagger).
\end{aligned} \tag{2}$$

Here all the Higgs fields are represented by two-by-two matrices, and they are real, namely

$$\epsilon H_i^* \epsilon = -H_i, \quad \text{where } \epsilon = \begin{pmatrix} 0 & 1 \\ -1 & 0 \end{pmatrix}. \tag{3}$$

All parameters in the Higgs potential are also real. We assume that all the vacuum expectation values (VEVs) of the Higgs fields are diagonal, real and positive to realize desired electroweak symmetry breaking. The Higgs fields are expanded around their VEVs,  $v_1$ ,  $v_2$  and  $v_3$ ,

$$H_i = \frac{v_i}{2} + \frac{1}{2} (h_i + i\tau^a \pi_i^a), \tag{4}$$

where  $\tau^a$  is the Pauli matrices, and  $h_i$ ,  $\pi_i^a$  are the four real scalar component fields. The covariant derivatives of the Higgs fields are given as

$$D_\mu H_1 = \partial_\mu H_1 + ig_0 \frac{\tau^a}{2} W_{0\mu}^a H_1 - ig_1 H_1 \frac{\tau^a}{2} W_{1\mu}^a, \tag{5}$$

---

<sup>#1</sup> We omit the term  $i\kappa' \text{tr}(H_1 H_2 H_3^\dagger \tau^3)$  in this paper because this term can be eliminated by the field redefinition [23].

$$D_\mu H_2 = \partial_\mu H_2 + ig_1 \frac{\tau^a}{2} W_{1\mu}^a H_2 - ig_2 H_2 \frac{\tau^3}{2} B_\mu, \quad (6)$$

$$D_\mu H_3 = \partial_\mu H_3 + ig_0 \frac{\tau^a}{2} W_{0\mu}^a H_3 - ig_2 H_3 \frac{\tau^3}{2} B_\mu. \quad (7)$$

By calculating the muon life time in this model at the tree level, we find the relation between the Fermi constant and the VEVs in this model as

$$v_3^2 + \frac{1}{\frac{1}{v_1^2} + \frac{1}{v_2^2}} = v^2 \equiv \left( \sqrt{2} G_F \right)^{-1}, \quad (8)$$

where  $v \simeq 246$  GeV. For the later convenience, we introduce a new parameter  $r$ ,

$$r \equiv \frac{v_2}{v_1}. \quad (9)$$

Thus  $v_1$  and  $v_2$  are expressed by  $r$ ,  $v_3$ , and  $v$ ,

$$v_1^2 = (1 + r^{-2})(v^2 - v_3^2), \quad v_2^2 = (1 + r^2)(v^2 - v_3^2). \quad (10)$$

There are twelve scalars in this model, and six of them are eaten by the gauge bosons. Thus this model has six physical scalars: three CP-even Higgs bosons ( $h$ ,  $H$ ,  $H'$ ), one CP-odd Higgs boson ( $A$ ), and two charged Higgs bosons ( $H^\pm$ ). We identify  $h$  as the SM-like 125 GeV Higgs bosons. The masses of the CP-odd and the charged Higgs bosons are the same at the tree level and given by

$$m_A^2 = m_{H^\pm}^2 = -\frac{1}{4} \frac{\kappa}{v_3} \frac{1 + r^2}{r} v^2. \quad (11)$$

The mass eigenstates of the CP-even Higgs bosons are related to the gauge eigenstates through the mixing angles  $\theta_1$ ,  $\theta_2$ , and  $\theta_3$  as follows,

$$\begin{pmatrix} H' \\ H \\ h \end{pmatrix} = \begin{pmatrix} s_1 s_2 - c_1 c_2 s_3 & -s_1 c_2 - c_1 s_2 s_3 & c_1 c_3 \\ -c_1 s_2 - s_1 c_2 s_3 & c_1 c_2 - s_1 s_2 s_3 & s_1 c_3 \\ c_2 c_3 & s_2 c_3 & s_3 \end{pmatrix} \begin{pmatrix} h_1 \\ h_2 \\ h_3 \end{pmatrix} \quad (12)$$

where  $s_i$  ( $c_i$ ) stands for  $\sin \theta_i$  ( $\cos \theta_i$ ) for  $i = 1, 2, 3$ .

The Yukawa interactions are given as

$$\mathcal{L}^{\text{Yukawa}} = -\bar{Q}^i H_3 \begin{pmatrix} y_u^{ij} & 0 \\ 0 & y_d^{ij} \end{pmatrix} \begin{pmatrix} u_R^j \\ d_R^j \end{pmatrix} - \bar{L}^i H_3 \begin{pmatrix} 0 & 0 \\ 0 & y_e^{ij} \end{pmatrix} \begin{pmatrix} 0 \\ e_R^j \end{pmatrix} + H.c., \quad (13)$$

where  $i$  and  $j$  are the generation indices. We introduce a parameter  $\kappa_F$  which is the ratio of the couplings between the lightest CP-even Higgs boson and the fermions to its SM value,

$$\kappa_F \equiv \frac{g_{hff}}{m_f/v} = \frac{v}{v_3} s_3. \quad (14)$$

Since  $|s_3| \leq 1$  and  $v/v_3 > 1$ ,  $\kappa_F$  can be larger than one. We will discuss the viable range of  $\kappa_F$  in the next subsection. The fermion masses are given as

$$m_f = y_f \frac{v_3}{2} = y_f \frac{v_3}{v} \frac{v}{2}, \quad (15)$$

and the Yukawa couplings are enhanced by  $v/v_3$  compared to their SM values. Large Yukawa couplings could make the Higgs potential unstable above the electroweak scale. We discuss this point in Sec. 3.2.

In addition to the SM gauge bosons, we have extra three vector bosons,  $W'^{\pm}$  and  $Z'$ . In the  $g_1 \gg g_0$  regime, the mass eigenvalues of the gauge bosons are given as

$$m_W^2 \simeq \frac{1}{4} g_0^2 v^2 \left( 1 - \frac{g_0^2}{g_1^2} \frac{1}{(1+r^2)^2} \right), \quad (16)$$

$$m_{W'}^2 \simeq \frac{1}{4} g_1^2 (v_1^2 + v_2^2) \left( 1 + \frac{g_0^2}{g_1^2} \frac{1}{(1+r^2)^2} \right), \quad (17)$$

$$m_Z^2 \simeq \frac{1}{4} (g_0^2 + g_2^2) v^2 \left( 1 - \frac{(g_0^2 - g_2^2 r^2)^2}{g_1^2 (g_0^2 + g_2^2)} \frac{1}{(1+r^2)^2} \right), \quad (18)$$

$$m_{Z'}^2 \simeq \frac{1}{4} g_1^2 (v_1^2 + v_2^2) \left( 1 + \frac{g_0^2 + g_2^2 r^4}{g_1^2} \frac{1}{(1+r^2)^2} \right). \quad (19)$$

We find  $m_{W'} \simeq m_{Z'}$  except in the large  $r$  regime. We need to find the relation between the gauge eigenstates and the mass eigenstates to evaluate the couplings, and they are given as

$$W_{\mu}^{\pm} \simeq \left( 1 - \frac{1}{2(1+r^2)^2} \frac{g_0^2}{g_1^2} \right) W_{0\mu}^{\pm} + \left( \frac{1}{1+r^2} \frac{g_0}{g_1} \right) W_{1\mu}^{\pm}, \quad (20)$$

$$W_{\mu}'^{\pm} \simeq - \left( \frac{1}{1+r^2} \frac{g_0}{g_1} \right) W_{0\mu}^{\pm} + \left( 1 - \frac{1}{2(1+r^2)^2} \frac{g_0^2}{g_1^2} \right) W_{1\mu}^{\pm}, \quad (21)$$

$$A_{\mu} = \frac{e}{g_0} W_{0\mu}^3 + \frac{e}{g_1} W_{1\mu}^3 + \frac{e}{g_2} W_{2\mu}^3, \quad (22)$$

$$\begin{aligned} Z_{\mu} &\simeq c_W \left( 1 - \frac{1 - 2r^2 t_W^2}{2(1+r^2)^2} \frac{g_0^2}{g_1^2} \right) W_{0\mu}^3 + c_W \left( \frac{1 - r^2 t_W^2}{(1+r^2)} \frac{g_0}{g_1} \right) W_{1\mu}^3 \\ &\quad - s_W \left( 1 - \frac{r^4 t_W^2}{2(1+r^2)^2} \frac{g_0^2}{g_1^2} \right) W_{2\mu}^3, \end{aligned} \quad (23)$$

$$Z'_{\mu} \simeq - \frac{1}{1+r^2} \frac{g_0}{g_1} W_{0\mu}^3 + \left( 1 - \frac{1 + r^4 t_W^2}{2(1+r^2)^2} \frac{g_0^2}{g_1^2} \right) W_{1\mu}^3 - \frac{r^2 t_W}{(1+r^2)} \frac{g_0}{g_1} W_{2\mu}^3, \quad (24)$$

where  $c_W = m_W/m_Z$ ,  $s_W = \sqrt{1 - c_W^2}$ , and  $t_W = s_W/c_W$ . The typical size of the mixing angles is  $\mathcal{O}(g_0/g_1)$ , and the gauge field  $W_0$  ( $W_1$ ) is the main component of the mass eigenstate  $W$  ( $W'$ ). It is worth noting that the mixing angles for  $W'$  and  $Z'$  become the same in the small  $r$  regime, which means the custodial symmetry is enhanced.

The approximate expressions for some couplings of the  $W'$  and  $Z'$  to the SM particles are given as

$$\frac{g_{W'ff}}{g_{Wff}^{\text{SM}}} \simeq -\frac{m_W}{m_{W'}} \sqrt{1 - \frac{v_3^2}{v^2}} \frac{1}{r}, \quad (25)$$

$$\frac{g_{W'WZ}}{g_{WWZ}^{\text{SM}}} \simeq -\frac{m_W}{m_{W'}} \sqrt{1 - \frac{v_3^2}{v^2}} \frac{1}{c_W^2} \frac{r}{1 + r^2}, \quad (26)$$

$$\frac{g_{WWZ'}}{g_{WWZ}^{\text{SM}}} \simeq -\frac{m_W}{m_{W'}} \sqrt{1 - \frac{v_3^2}{v^2}} \frac{1}{c_W} \frac{r}{1 + r^2}. \quad (27)$$

Compare to the benchmark model (sequential standard model (SSM) [29–31]) used by the ATLAS/CMS, the  $W'$  couplings to the SM fermions are smaller. All couplings have a suppression factor of  $(m_W/m_{W'})\sqrt{1 - v_3^2/v^2}$ , because the  $W'$  boson couples to the elementary fermion through  $W_0$ - $W_1$  mixing, so that the width is narrow. Since  $g_{W'ff}$  is proportional to  $r^{-1}$ , the production cross section of the Drell-Yan process is proportional to  $r^{-2}$ . The  $W'$  boson could not be produced in the large  $r$  region. In Sec. 3, we will find a parameter space in small  $r$  regions where a signal rate is consistent with the ATLAS diboson excess. Some numerical results are given in Sec. 3.3

The gauge boson couplings to the scalars are also important in our analysis. We give their approximated expressions here. Due to the mixing between the two SU(2) gauge eigenstates, the  $WWh$  and  $ZZh$  couplings differ from the SM values. We denote these coupling ratios to the SM values by  $\kappa_{W,Z}$ ,

$$\kappa_W \equiv \frac{g_{hWW}}{2m_W^2/v}, \quad \kappa_Z \equiv \frac{g_{hZZ}}{2m_Z^2/v}, \quad (28)$$

and their approximated formulae in the  $g_1 \gg g_0, g_2$  regime are

$$\kappa_W \simeq \kappa_Z \simeq \frac{r^3}{(1 + r^2)^{3/2}} \sqrt{1 - \frac{v_3^2}{v^2}} c_2 c_3 + \frac{1}{(1 + r^2)^{3/2}} \sqrt{1 - \frac{v_3^2}{v^2}} s_2 c_3 + \frac{v_3}{v} s_3. \quad (29)$$

The couplings relevant to the  $W'/Z'$  decay are

$$g_{WW'h} \simeq g_{ZZ'h} \simeq \frac{2m_W m_{W'}}{v} \left( -\frac{r^2}{(1 + r^2)^{3/2}} c_2 c_3 + \frac{r}{(1 + r^2)^{3/2}} s_2 c_3 - \frac{1}{r} \frac{m_W^2}{m_{W'}^2} \frac{v_3}{v} \sqrt{1 - \frac{v_3^2}{v^2}} s_3 \right), \quad (30)$$

$$\begin{aligned} g_{WW'H} \simeq g_{ZZ'H} \simeq & \frac{2m_W m_{W'}}{v} \left( -\frac{r^2}{(1 + r^2)^{3/2}} (-c_1 s_2 - s_1 c_2 s_3) \right. \\ & \left. + \frac{r}{(1 + r^2)^{3/2}} (c_1 c_2 - s_1 s_2 s_3) - \frac{1}{r} \frac{m_W^2}{m_{W'}^2} \frac{v_3}{v} \sqrt{1 - \frac{v_3^2}{v^2}} s_1 c_3 \right), \end{aligned} \quad (31)$$

$$g_{WW'H'} \simeq g_{ZZ'H'} \simeq \frac{2m_W m_{W'}}{v} \left( -\frac{r^2}{(1+r^2)^{3/2}} (s_1 s_2 - c_1 c_2 s_3) + \frac{r}{(1+r^2)^{3/2}} (-s_1 c_2 - c_1 s_2 s_3) - \frac{1}{r} \frac{m_W^2}{m_{W'}^2} \frac{v_3}{v} \sqrt{1 - \frac{v_3^2}{v^2}} c_1 c_3 \right). \quad (32)$$

## 2.2 Model parameters

In the electroweak sector of the model, there are 13 real parameters,

$$\mu_1^2, \mu_2^2, \mu_3^2, \kappa, \lambda_1, \lambda_2, \lambda_3, \lambda_{12}, \lambda_{23}, \lambda_{31}, g_0, g_1, g_1. \quad (33)$$

It is convenient to use a different set of the parameters instead of these parameters. We use the following 13 parameters to fix the parameters in the electroweak sector,

$$r, v_3, v, \alpha, m_Z, m_{Z'}, m_h, m_{H'}, m_H, m_A, \kappa_F, \kappa_Z, g_{WW'H'}. \quad (34)$$

Here, we use  $r, v_3, v$  instead of the three  $\mu$  parameters.  $\kappa$  is fixed by the charged Higgs mass or the CP-odd Higgs mass. The six  $\lambda$ 's have the same information as the three CP-even Higgs masses and their mixing angles ( $m_h, m_H, m_{H'}, \theta_1, \theta_2, \theta_3$ ). We can use  $m_Z, m_{Z'}$ , and  $\alpha (= e^2/4\pi)$  instead of the gauge couplings. In addition, we can replace ( $\theta_1, \theta_2, \theta_3$ ) with ( $\kappa_F, \kappa_Z, g_{WW'H'}$ ).

The values of the four parameters,  $v, m_Z, \alpha$ , and  $m_h$  are already known very precisely. We take  $m_h = 125$  GeV. We find  $\kappa_F$  is severely constrained close to 1 in the  $m_A \gg m_h$  regime. When the heavy Higgs masses are universal,  $m_A = m_{H'} = m_H$ ,  $\lambda_3$  is simply expressed as

$$\lambda_3(\mu = m_{Z'}) = \frac{\kappa_F^2 m_h^2}{2 v^2} + \frac{1 - \kappa_F^2 m_A^2}{2 v^2}. \quad (35)$$

Thus,  $\lambda_3$  is very large except for  $\kappa_F = 1$ . Similarly, the coupling ratio  $\kappa_Z$  is also severely constrained close to its maximal value in  $m_A \gg m_h$  regime. Typically, the allowed value of  $\kappa_Z$  is  $1 - \mathcal{O}(1)\%$ . The detailed description is given in Appendix A. In the following discussion, we take  $\kappa_F \simeq 1$ ,  $m_A = m_H = m_{H'} = \mathcal{O}(1)$  TeV,  $g_{WW'H'} = 0$ , and we always choose  $\kappa_Z$  to be its maximal value. For most of our numerical analysis,  $\kappa_Z$  is set to 0.95–1.00.

## 3 Phenomenology of spin-1 resonances

In this section, we discuss the properties of the  $W'$  and  $Z'$  bosons such as the production cross sections and the decay branching ratios. And we also discuss both the theoretical and experimental constraints. In the following, we show some formulae with approximation, which help to understand the parameter dependence. However, we use the exact formulae in our numerical calculations.

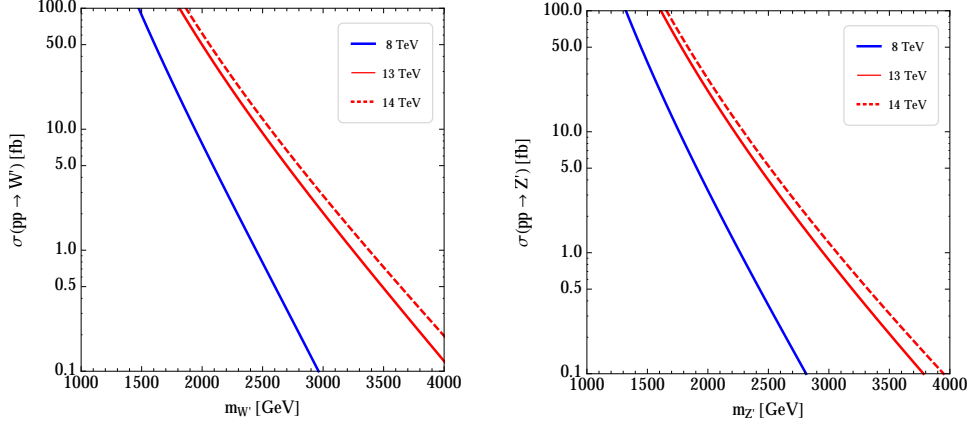


Figure 2. The production cross sections of the extra vector bosons,  $W'$  and  $Z'$ . We take  $v_3 = 200$  GeV,  $r = 0.13$ .

### 3.1 Properties of the extra vector bosons

The main production mode of  $W'$  and  $Z'$  in  $pp$  collisions is the Drell-Yan process. They are proportional to  $r^{-2}$  as we can see from Eq. (25).<sup>#2</sup> We consider small  $r$  in order to make the cross section large. In Fig. 2, we show the production cross sections for  $W'$  ( $W'^+ + W'^-$ ) and  $Z'$ . Here we take  $v_3 = 200$  GeV,  $r = 0.13$  and  $\kappa_F = 1.00$ . We use the CTEQ6L parton distribution functions [32]. The production cross section of  $W'$  is approximately twice that of  $Z'$  for small  $r$  because the custodial  $SU(2)$  symmetry is recovered in the region.

The partial decay widths of  $W'$  and  $Z'$  into the SM particles are given as

$$\Gamma(W' \rightarrow WZ) \simeq \frac{1}{48\pi} \frac{m_{W'}^3}{v^2} \frac{r^2}{(1+r^2)^2} \left(1 - \frac{v_3^2}{v^2}\right), \quad (36)$$

$$\Gamma(W' \rightarrow Wh) \simeq \frac{1}{48\pi} \frac{m_{W'}^3}{v^2} \frac{r^2}{(1+r^2)^3} (-rc_2c_3 + s_2c_3)^2, \quad (37)$$

$$\Gamma(W' \rightarrow f\bar{f}) \simeq \frac{N_c}{48\pi} \frac{m_W^2}{m_{W'}} \frac{e^2}{s_W^2} \frac{1}{r^2} \left(1 - \frac{v_3^2}{v^2}\right), \quad (38)$$

$$\Gamma(Z' \rightarrow WW) \simeq \frac{1}{48\pi} \frac{m_{W'}^3}{v^2} \frac{r^2}{(1+r^2)^2} \left(1 - \frac{v_3^2}{v^2}\right), \quad (39)$$

$$\Gamma(Z' \rightarrow Zh) \simeq \frac{1}{48\pi} \frac{m_{W'}^3}{v^2} \frac{r^2}{(1+r^2)^3} (-rc_2c_3 + s_2c_3)^2, \quad (40)$$

$$\Gamma(Z' \rightarrow f\bar{f}) \simeq \frac{N_c}{24\pi} \frac{m_W^2}{m_{W'}} \frac{e^2}{s_W^2} \frac{1}{r^2} \left(1 - \frac{v_3^2}{v^2}\right)$$

<sup>#2</sup>For more details on the formulae, see Appendix B.

$$\times \left( \left( \left( 1 - r^2 \frac{s_W^2}{c_W^2} \right) T_f^3 + r^2 \frac{s_W^2}{c_W^2} Q_f \right)^2 + \left( r^2 \frac{s_W^2}{c_W^2} Q_f \right)^2 \right), \quad (41)$$

where  $T_f^3 = 1/2$  ( $-1/2$ ) for the up-type (down-type) fermions,  $Q_f$  is the electric charge of the fermion, and  $N_c$  is the color factor,  $N_c = 3$ . Note that the bosonic channels are dominant among their decay channels due to an enhancement factor from the wave function of the longitudinally polarized gauge bosons in the final states. Therefore the dominant decay modes of  $W'$  ( $Z'$ ) are  $W' \rightarrow WZ$  and  $W' \rightarrow Wh$  ( $Z' \rightarrow WW$  and  $Z' \rightarrow Zh$ ).

There are also decay modes with a heavy scalar in the final states. For example,  $W' \rightarrow WH$  and  $W' \rightarrow hH$  exist and their approximated formulae are

$$\Gamma(W' \rightarrow WH) \simeq \frac{1}{48\pi} \left( \frac{g_{WW'H}}{2m_W m_{W'}/v} \right)^2 \frac{m_{W'}^3}{v^2} \left( 8 \frac{m_W^2}{m_{W'}^2} + \left( 1 - \frac{m_H^2}{m_{W'}^2} + \frac{m_W^2}{m_{W'}^2} \right)^2 \right) \left( 1 - \frac{m_H^2}{m_{W'}^2} \right), \quad (42)$$

$$\Gamma(W' \rightarrow hH) \simeq \frac{1}{48\pi} \frac{m_{W'}^4}{v^2 - v_3^2} \frac{v_3^2}{v^2} \frac{2}{(1+r^2)^3} (-rc_2c_3 + s_2c_3)^2 \left( 1 - \frac{m_{H^+}^2}{m_{W'}^2} \right)^3, \quad (43)$$

where  $g_{WW'H}$  is given in Eq. (31), and  $g_{WW'H}/(2m_W m_{W'}/v)$  is  $\mathcal{O}(1)$  in large regions of the parameter space. These decay widths are comparable to those of the SM final states. The decay channels including only the heavy states, such as  $W' \rightarrow H^\pm H$ , also have the same feature. Once these modes are open, they would be dominant decay modes.

In Fig. 3, we show the total widths and the branching ratios of  $W'$  and  $Z'$ . Here we take  $v_3 = 200$  GeV,  $r = 0.13$  and  $\kappa_F = 1.00$ ,  $m_A = m_{H'} = m_H = 2$  TeV. We also take  $g_{WW'H'} = 0$  as we mentioned in Sec. 2.2, thus  $W' \rightarrow WH'$  and  $Z' \rightarrow ZH'$  are absent in the figure. We find that the dominant decay channels are  $V' \rightarrow VV$  and  $V' \rightarrow Vh$  for large  $m_{V'}$ . However, the decay branching ratio reduces once  $V' \rightarrow HX$  decay modes are open.

In Fig. 3, we find  $\text{Br}(W' \rightarrow WZ) = \text{Br}(W' \rightarrow Wh) \simeq 40\%$  at  $m_{W'} = 2$  TeV. The relation is easily understood by the equivalence theorem,  $\text{Br}(W' \rightarrow W_L Z_L) = \text{Br}(W' \rightarrow \pi_{SM} \pi_{SM})$  in the heavy  $W'$  mass limit, where  $\pi_{SM}$  is the SM Nambu-Goldstone boson. In the SM limit,  $\text{Br}(W' \rightarrow \pi_{SM} \pi_{SM})$  is equivalent to  $\text{Br}(W' \rightarrow \pi_{SM} h)$ . Thus,  $\text{Br}(W' \rightarrow WZ) \simeq \text{Br}(W' \rightarrow Wh)$  is realized. In addition, when one takes  $g_{WW'H'} = 0$ , the heavy Higgses  $H$ ,  $A$ ,  $H^\pm$  form a multiplet, and  $\text{Br}(W' \rightarrow ZH^\pm) \simeq \text{Br}(W' \rightarrow WA) \simeq \text{Br}(W' \rightarrow WH)$  is realized.

We also find the total widths are narrow, namely  $\Gamma/m \sim 1\text{--}5\%$ , because the resonances decay into the SM particles with suppressed couplings due to the mixing between the elementary and the composite sectors. Another remark is that the decay properties of  $W'$  and  $Z'$  are similar due to the enhanced  $\text{SU}(2)$  custodial symmetry in small  $r$  regime.<sup>#3</sup>

---

<sup>#3</sup>In the large  $r$  region, the branching ratio  $Z' \rightarrow f\bar{f}$  and the production cross section of  $Z'$  become larger (see Eqs. (41, 72)), while the production cross section of  $W'$  is suppressed.

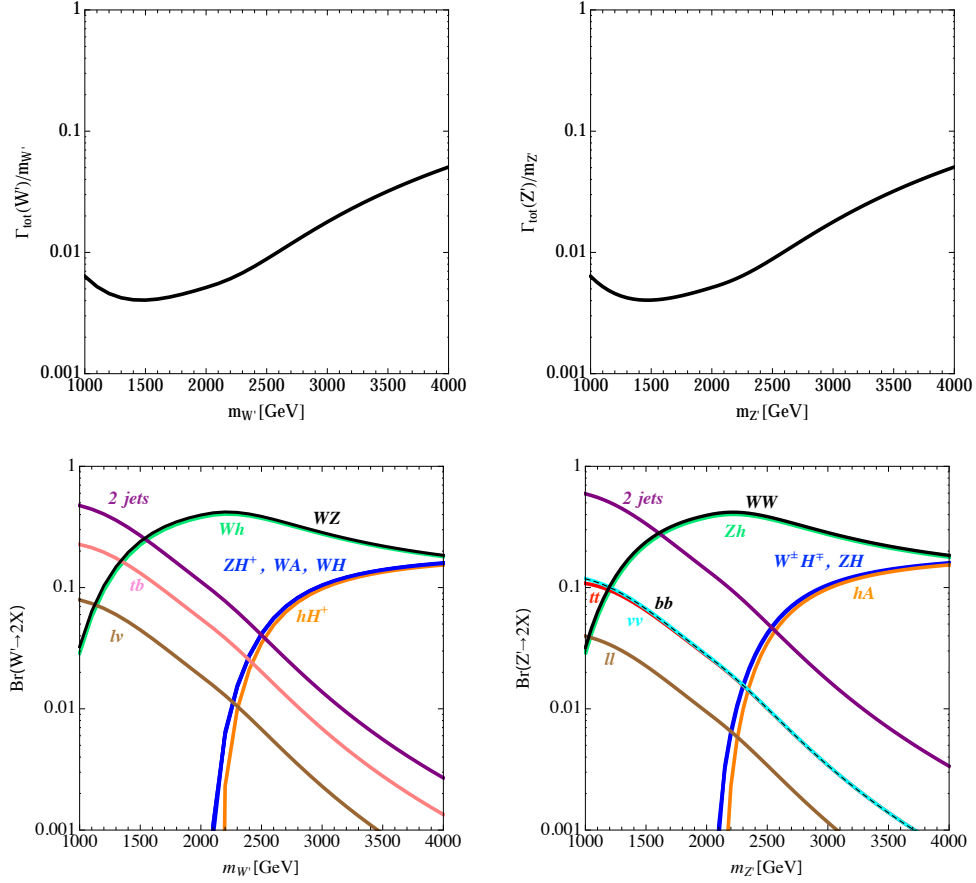


Figure 3. The total widths and the branching ratios of the extra vector bosons,  $W'$  and  $Z'$ . We take  $v_3 = 200$  GeV,  $r = 0.13$ ,  $\kappa_F = 1.00$ , and  $m_A = m_{H'} = m_H = 2$  TeV. Here, 2jets means  $\text{Br}(W' \rightarrow ud) + \text{Br}(W' \rightarrow sc)$  or  $\text{Br}(Z' \rightarrow uu) + \text{Br}(Z' \rightarrow dd) + \text{Br}(Z' \rightarrow ss) + \text{Br}(Z' \rightarrow cc)$ ,  $\ell\nu$  means  $\text{Br}(W' \rightarrow e\nu_e)$  ( $=\text{Br}(W' \rightarrow \mu\nu_\mu) = \text{Br}(W' \rightarrow \tau\nu_\tau)$ ),  $\ell\ell$  means  $\text{Br}(Z' \rightarrow ee)$  ( $=\text{Br}(Z' \rightarrow \mu\mu) = \text{Br}(Z' \rightarrow \tau\tau)$ ),  $\nu\nu$  means  $\text{Br}(Z' \rightarrow \nu_e\nu_e) + \text{Br}(Z' \rightarrow \nu_\mu\nu_\mu) + \text{Br}(Z' \rightarrow \nu_\tau\nu_\tau)$ , and  $W^\pm H^\mp$  means  $\text{Br}(W' \rightarrow W^+ H^-) = \text{Br}(W' \rightarrow W^- H^+)$ .



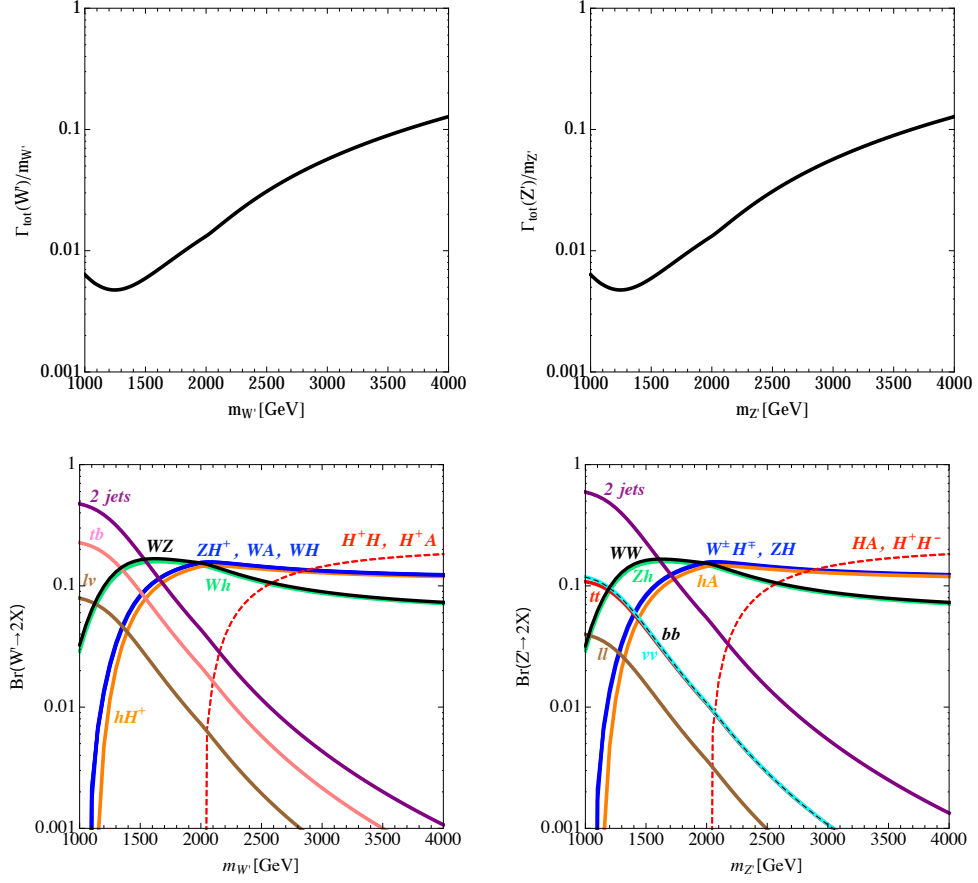


Figure 4. The total widths and the branching ratios of  $W'$  and  $Z'$  for  $m_A = m_{H'} = m_H = 1$  TeV. Other parameter choice and the notations are the same as in Fig. 3.

In Fig. 4, we take different scalar masses,  $m_A = m_{H'} = m_H = 1$  TeV. The other parameter choice is the same as in Fig. 3. The decay channels to the non-SM particles, namely  $\text{Br}(W' \rightarrow H^+H)$ ,  $\text{Br}(W' \rightarrow H^+A)$ ,  $\text{Br}(Z' \rightarrow HA)$ , and  $\text{Br}(Z' \rightarrow H^+H^-)$ , are open. We took the parameter so that the channels to  $H'$  is absent,  $g_{WW'H'} = 0$ .

As mentioned above, these channels are comparable to the decay modes to the SM particles. As a result, the decay modes  $V' \rightarrow VV$  and  $V' \rightarrow Vh$  searched at the ATLAS and the CMS experiments are suppressed compared to Fig. 3. This implies that the decay channels with heavy scalars should not be open if we try to explain the excess at the ATLAS experiment. Hereafter, we consider the situation that the heavy scalars are as heavy as the extra gauge bosons.

## 3.2 Constraints on the model

In this subsection, we show theoretical and experimental constraints on the model parameters. In order to perform a reliable perturbative calculation, we demand perturbativity condition, bounded below condition, global minimum vacuum condition, and stability condition. In addition, we take into account the LHC bounds and the electroweak precision measurements.

### 3.2.1 Theoretical constraints

#### Perturbativity condition for the gauge coupling $g_1$

We require that all the absolute values of the gauge couplings and the Higgs quartic couplings are smaller than  $4\pi$  and  $(4\pi)^2$  in order to keep the reliability of our analysis based on the perturbative calculation.

For the gauge couplings,  $g_0$  and  $g_2$  are almost the same value as the SM gauge couplings, but  $g_1$  can be very large. Since  $\text{SU}(2)_1$  is asymptotic free in our setup,  $g_1$  becomes smaller at high energy due to the quantum effects. Thus the maximum value of the  $g_1$  is given at  $Z'$  mass scale, and we require  $|g_1(\mu = m_{Z'})| < 4\pi$ . The regions where  $|g_1(m_{Z'})| > 4\pi$  are filled with yellow in Figs. 5 and 6.

#### Perturbativity condition for the Higgs quartic couplings

The scalar quartic couplings are large when the mass differences between the SM-like Higgs and the other heavy scalar bosons are large. Since we take  $m_h \ll m_A = m_H = m_{H'} \sim \mathcal{O}(1)$  TeV in our analysis, the quartic couplings tend to be large. In addition, due to the renormalization group effects, they can be even larger at high energy. The renormalization group equations for this model are given in Appendix C. We define a cutoff scale  $\Lambda$  by

$$|\lambda_i(\mu = \Lambda)| = (4\pi)^2, \quad (44)$$

and require  $|\lambda_i(\mu < \Lambda)| < (4\pi)^2$ .

This constraint highly depends on our choice of  $\Lambda$ . We require that  $\Lambda$  should be significantly higher than a few TeV, otherwise we have to take account of interaction terms from higher dimensional operators whose coefficients are unknown, and some uncertainty is introduced to our analysis. For example, there are operators which modifies the  $W'$  coupling to the SM fermions such as  $(c/\Lambda^2)\bar{Q}i\gamma^\mu(H_1iD_\mu H_1^\dagger)Q$ . This operator brings unknown parameter  $c$ , and thus brings uncertainty to our calculations such as the production cross section of  $W'$ . Typically, such higher dimensional operators with  $c \sim 1$  bring 1% (10%) uncertainty if  $\Lambda = 100$  TeV (10 TeV). To avoid such uncertainty from unknown parameters, we restrict ourselves for the case  $\Lambda > 100$  TeV. The parameter regions where  $|\lambda(\Lambda)| > (4\pi)^2$  are filled with the lighter (darker) gray for  $\Lambda = 100$  (10) TeV in Figs. 5 and 6 for reference.

### Bounded below condition

Here we consider the conditions that the Higgs potential at the tree level is bounded below. For the purpose, it is enough to check that the potential value at the large field values, and thus we consider only the quartic terms in the potential. We rewrite the quartic terms as

$$V_{\text{quartic}} = R^4 (\lambda_1 n_1^2 + \lambda_2 n_2^2 + \lambda_3 n_3^2 + \lambda_{12} n_1 n_2 + \lambda_{23} n_2 n_3 + \lambda_{31} n_3 n_1), \quad (45)$$

with

$$R^2 n_i \equiv \text{tr}(H_i H_i^\dagger) = \frac{1}{2}(h_i^2 + \pi_i^a \pi_i^a), \quad (46)$$

where  $n_i$  satisfies  $0 \leq n_{1,2,3} \leq 1$ , and  $n_1^2 + n_2^2 + n_3^2 = 1$ . In order to avoid run-away vacua, we demand the following conditions for the Higgs quartic couplings at  $m_{Z'}$  scale ( $\lambda_i(\mu = m_{Z'})$ ),

$$\text{Min} [\lambda_1 n_1^2 + \lambda_2 n_2^2 + \lambda_3 n_3^2 + \lambda_{12} n_1 n_2 + \lambda_{23} n_2 n_3 + \lambda_{31} n_3 n_1] > 0, \quad \text{for } 0 \leq n_{1,2,3} \leq 1. \quad (47)$$

The parameter regions where this condition is not satisfied are filled with cyan in Figs. 5 and 6. Especially, one can solve the above inequality analytically in specific directions as

$$\begin{aligned} \lambda_1 > 0 \quad \text{for } n_2 = n_3 = 0, & \quad \lambda_2 > 0 \quad \text{for } n_1 = n_3 = 0, \\ \lambda_3 > 0 \quad \text{for } n_1 = n_2 = 0, & \quad \lambda_{23} + 2\sqrt{\lambda_2 \lambda_3} > 0 \quad \text{for } n_1 = 0, \\ \lambda_{31} + 2\sqrt{\lambda_3 \lambda_1} > 0 \quad \text{for } n_2 = 0, & \quad \lambda_{12} + 2\sqrt{\lambda_1 \lambda_2} > 0 \quad \text{for } n_3 = 0. \end{aligned} \quad (48)$$

### Global minimum vacuum condition

We demand the electroweak vacuum to be a global minimum of the Higgs potential at  $\mu = m_{Z'}$ . The parameter regions where this condition is not satisfied are filled with green in Figs. 5 and 6.

## Stability condition

Among the quartic couplings,  $\lambda_3$  can be very small when  $\kappa_F$  is very close to 1, see Eq. (35), and especially it takes the same value as the quartic coupling in the SM for  $\kappa_F = 1$ . In that case,  $\lambda_3$  can be negative at a high energy scale due to the contribution from the Yukawa interaction to the renormalization group equations, and the Higgs potential becomes unstable. The VEV giving masses to the fermions are  $v_3$ , see Eq. (15). Thus the Yukawa coupling in our setup is larger than the coupling in the SM by  $v/v_3$ , and the Higgs potential can become unstable at a few TeV scale for the small  $v_3$  region. We define the scale  $\bar{\Lambda}$  at which  $\lambda_3$  becomes negative,

$$\lambda_3(\mu = \bar{\Lambda}) = 0, \quad (49)$$

and we demand  $\bar{\Lambda} \gtrsim 100 \text{ TeV}$ , as we demand for the perturbativity condition. We fill the regions where this condition is not satisfied with magenta in Figs. 5 and 6.

This bound is conservative because we do not allow a meta-stable vacuum. Note that we do not take into account higher loop corrections. In the SM, the constraints become significantly weaker if higher loop corrections are taken into account [33, 34].

## 3.2.2 Experimental constraints

### Constraints from the direct search for $W'$ and $Z'$

Since the production cross sections of the extra vector bosons are relatively large, this model is constrained from current results of the exotic resonance searches of various decay channels at the  $\sqrt{s} = 8 \text{ TeV}$  LHC. We take account of the following constraints:  $W' \rightarrow \ell\nu$  searches [35, 36],  $Z' \rightarrow \ell\ell$  searches [37, 38],  $Vh$  resonance searches ( $V' \rightarrow Vh$ ) [39–42], and the diboson searches ( $V' \rightarrow VV$ ) using dijets [1, 2],  $\ell\ell jj$  [43],  $\ell\nu jj$  [44], and  $\ell\nu\ell\ell$  channel [45]. The searches for the other channels do not constrain this model. We fill the excluded regions with blue in Figs. 5 and 6. Among the constraints,  $V' \rightarrow Vh$  and  $V' \rightarrow WZ \rightarrow \ell\nu jj$  give severe bound, and exclude a part of the parameter regions in which we can explain the diboson excess reported by the ATLAS experiment.

### Constraints from the electroweak precision measurements

The electroweak precision parameters,  $\hat{S}$ ,  $\hat{T}$ ,  $W$  and  $Y$ , defined in Ref. [46], are severely restricted from the electroweak precision observables. Since the interactions of  $W'$  and  $Z'$  to the light fermions affect the low energy observables, the light  $W'$  and  $Z'$  are severely constrained. They are calculated at the tree level in Ref. [23],

$$\hat{S} = \frac{g_0^2 v_1^2 v_2^2}{g_1^2 (v_1^2 + v_2^2)^2 + g_0^2 v_1^4} \simeq \frac{m_W^2}{m_{W'}^2} \left( 1 - \frac{v_3^2}{v^2} \right), \quad (50)$$

$$\hat{T} = 0, \quad (51)$$

$$W = 4m_W^2 \frac{g_0^2}{g_1^2} \frac{1}{v_1^2 + v_2^2} \frac{v_1^4}{g_1^2(v_1^2 + v_2^2)^2 + g_0^2 v_1^4} \simeq \frac{m_W^4}{m_{W'}^4} \frac{1}{r^2} \left(1 - \frac{v_3^2}{v^2}\right), \quad (52)$$

$$Y = 4m_W^2 \frac{g_2^2}{g_1^2} \frac{1}{v_1^2 + v_2^2} \frac{v_2^4}{g_1^2(v_1^2 + v_2^2)^2 + g_0^2 v_1^4} \simeq r^2 t_W^2 \frac{m_W^4}{m_{W'}^4} \left(1 - \frac{v_3^2}{v^2}\right). \quad (53)$$

We use them to find the constraint on the parameter space. The parameter regions constrained at 95% C.L. are filled with red in Figs. 5 and 6. The small  $v_3$ , the small  $r$  as well as the light  $W'$  regions are constrained.

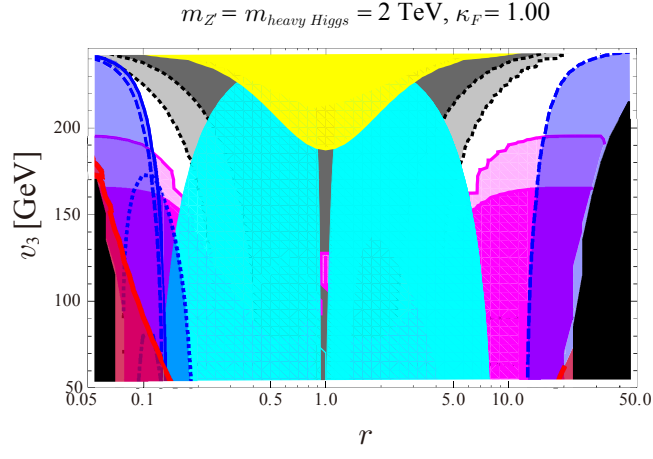
We also consider constraints from flavor physics, and find they are weaker than the constraints from  $\hat{S}$  and/or the current LHC bound. For example,  $K^0$ - $\bar{K}^0$  mixing in this model is almost the same as that in the SM. This is because the contributions from  $W'$  is sufficiently suppressed due to the suppression of the couplings to the SM fermions, and also the modification of the  $W$  couplings to the fermions is very small,  $\mathcal{O}(m_W^4/m_{W'}^4)$ . Therefore, we do not show the constraints in the figures.

### 3.2.3 Summary of the constraints

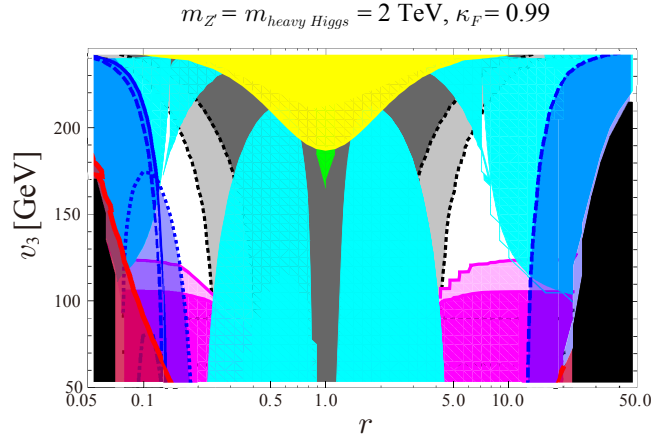
In Fig. 5, we plot all the constraints in  $r$ - $v_3$  planes with three different parameter sets,  $(m_{Z'}, m_A, \kappa_F) = (2 \text{ TeV}, 2 \text{ TeV}, 1.00)$ ,  $(2 \text{ TeV}, 2 \text{ TeV}, 0.99)$ , and  $(2 \text{ TeV}, 1 \text{ TeV}, 1.00)$ . Here we take all the heavy scalar bosons are degenerate,  $m_A = m_{H'} = m_H$ . The colored regions are excluded or constrained, and the white regions are allowed from all constraints. The gray regions surrounded by the black dotted lines represent the perturbativity condition of the Higgs quartic couplings for  $\Lambda = 10$  (darker) and 100 TeV (lighter), and the yellow regions are that of  $g_1$ . The bounded below condition excludes the cyan region. The global minimum vacuum condition excludes the green region. The magenta regions are excluded by the stability condition for  $\bar{\Lambda} = 10$  (darker) and 100 TeV (lighter). The LHC results exclude blue regions, where the solid blue lines represent  $W' \rightarrow \ell\nu$  searches [35, 36], the dashed lines represent  $Z' \rightarrow \ell\ell$  searches [37, 38], the dotted lines represent  $Vh$  resonance searches [39–42], and the dot-dashed lines represent diboson searches ( $V' \rightarrow VV$ ) [1, 2, 43–45]. The regions filled with the red color are excluded by the electroweak precision measurements. No physical solutions are found in the black region, namely the gauge couplings and/or the VEVs become complex numbers there.

By comparing all the panels, we find the experimental bounds (the LHC and the electroweak precision measurements) are almost insensitive to the heavy Higgs bosons. The theoretical bounds are very sensitive to the  $\kappa_F$ , as we can see from the panels (a) and (b). This is because the deviation of  $\kappa_F$  from 1 leads to the large  $\lambda_3$  (cf.  $\lambda_3 \sim 0.13$  (0.78) at  $\kappa_F = 1.00$  (0.99)) (see Eq. (35)), which changes the regions excluded by the bounded below condition (see Eq. (48)) and stability condition (see Eq. (49)). We find that perturbativity condition is weaker in the panel (c) ( $m_A = 1 \text{ TeV}$ ) compared with the panel (a) ( $m_A = 2 \text{ TeV}$ ). This is because the lighter  $m_A$  leads to the smaller quartic couplings.

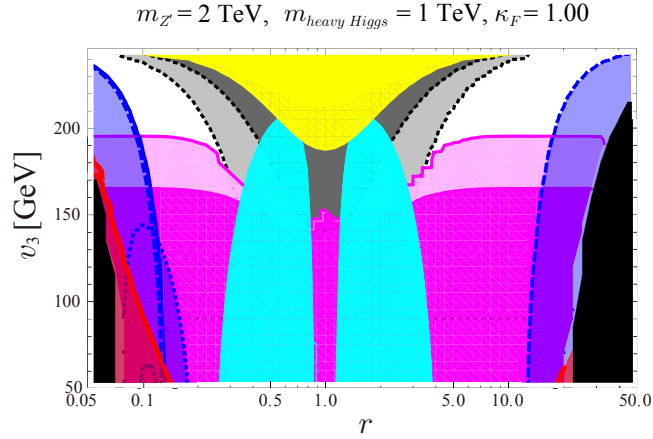
Figure 6 shows the constraints in  $m_{Z'}$ - $r$  plane with the same color notation in Fig. 5. We take the universal masses  $m_{Z'} = m_A = m_{H'} = m_H$ , and three different choices for  $v_3$



(a)



(b)



(c)

Figure 5. The theoretical and experimental constraints in  $r$ - $v_3$  planes. We take three different parameter choices for  $(m_{Z'}, m_A, \kappa_F)$ . The colored regions are constrained, **Gray**: the perturbativity conditions for the Higgs quartic couplings, **Yellow**: the perturbativity conditions for  $g_1$ , **Cyan**: the bounded below condition, **Green**: the global minimum vacuum condition, **Magenta**: the stability condition, **Blue**: the LHC bounds, **Red**: constraints from the electroweak precision measurements, **Black**: no physical solutions. See also the explanations in the text.

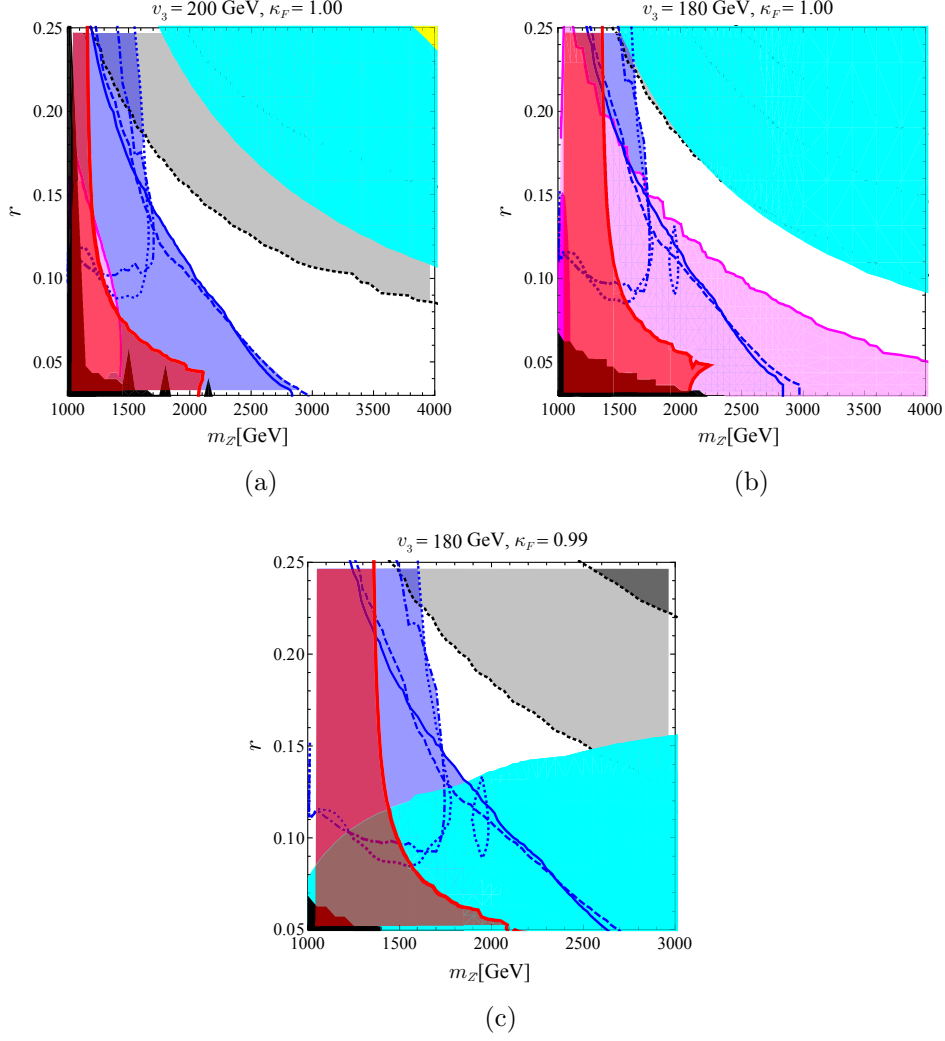


Figure 6. The theoretical and experimental constraints in the  $m_{Z'}$ - $r$  planes. We take three different parameter choices for  $(v_3, \kappa_F)$ , and the universal masses  $m_{Z'} = m_A = m_{H'} = m_H$  are taken. A color notation is the same as in Fig. 5.

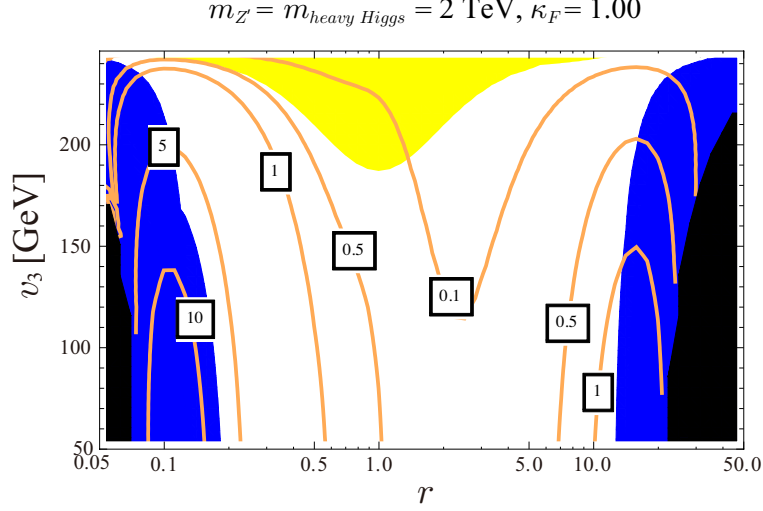


Figure 7. Contours of the cross section  $\sigma(pp \rightarrow W')\text{Br}(W' \rightarrow WZ) + \sigma(pp \rightarrow Z')\text{Br}(Z' \rightarrow WW)$  at the LHC  $\sqrt{s} = 8 \text{ TeV}$  in  $fb$  unit. We take  $m_{Z'} = m_A = m_{H'} = m_H = 2 \text{ TeV}$ ,  $\kappa_F = 1.00$ . The blue regions are excluded by the current experimental bounds, and the regions of  $g_1(\mu = m_{Z'}) > 4\pi$  are filled with yellow.

and  $\kappa_F$ ,  $(v_3, \kappa_F) = (200 \text{ GeV}, 1.00)$ ,  $(180 \text{ GeV}, 1.00)$ , and  $(180 \text{ GeV}, 0.99)$ . The perturbativity condition for the Higgs quartic couplings gives severe bounds in the heavy Higgs mass region. This is because the large mass differences in the CP-even Higgs mass spectra require the large Higgs quartic couplings, and they become non-perturbative eventually. We also find in the panel (c) that when  $\kappa_F$  deviates from 1, the bounded below condition gives stringent constraint. This is because that the Higgs quartic couplings  $\lambda_i$  are sensitive to the small deviation of  $\kappa_F$ , see Appendix A.

### 3.3 Current status: 8 TeV analyses

In this subsection, we focus on the cross section times branching ratios of  $V'$  at the LHC 8 TeV. Inspired by the recent ATLAS diboson excess [1], we concentrate on the case that the masses of the extra vector bosons are around 2 TeV.

Since the separation of the  $WW$ ,  $WZ$ , and  $ZZ$  channels are not good and there are significant overlap among them [1], we investigate the total cross section  $\sigma(pp \rightarrow W')\text{Br}(W' \rightarrow WZ) + \sigma(pp \rightarrow Z')\text{Br}(Z' \rightarrow WW)$  at  $\sqrt{s} = 8 \text{ TeV}$  in Fig. 7. In this figure,  $m_{Z'} = m_A = m_{H'} = m_H = 2 \text{ TeV}$ ,  $\kappa_F = 1.00$  are taken. The blue regions are excluded by the current experimental bounds discussed in Sec. 3.2, and the regions of  $g_1(\mu = m_{Z'}) > 4\pi$  is filled with yellow. Here we do not show the constraints from the Higgs sector.

We have to estimate the cross section value,  $\sigma(pp \rightarrow V' \rightarrow VV)$ , required for the explanation of the diboson excess. We find  $\sigma = 6 \text{ fb}$  with large error when we use the



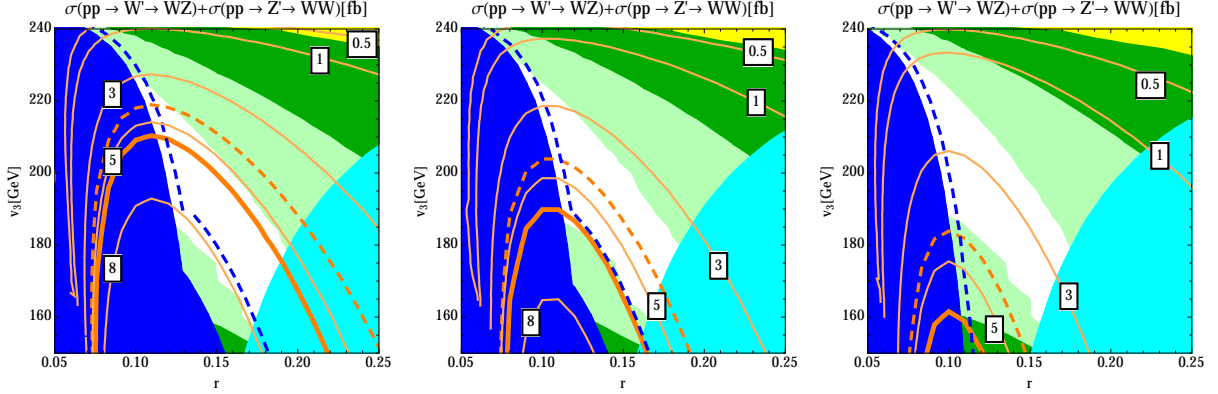


Figure 8. The cross sections of  $W'$  and  $Z'$  with two gauge bosons in their final states. We take  $m_{Z'} = 1.9$  TeV (the left panel), 2.0 TeV (the middle panel), and 2.1 TeV (the right panel). The color filled regions are excluded or constrained. The blue regions are excluded by the experimental bounds. The regions of  $g_1(\mu = m_{Z'}) > 4\pi$  are represented by yellow. The cyan regions are excluded by the bounded below condition. The green regions are constrained from the perturbativity and stability conditions where their cut off scale is 100 (10) TeV in the lighter green (darker green) regions. Below the thick orange line the cross section  $\sigma(pp \rightarrow V' \rightarrow VV)$  is consistent with the ATLAS result. After taking account of the  $K$ -factor, the boundaries of the regions change into the dashed orange lines, and the regions below the dashed blue lines are excluded by the LHC bounds.

event numbers between 1.85 and 2.15 TeV bins, the estimated background, and the efficiency given in Ref. [1]. Hereafter we require  $\sigma = 6$  fb for the explanation of the diboson excess.

This cross section value can be achieved in the regions where  $r$  is much smaller than 1. This is because the production cross section is enhanced by  $r^{-2}$ . Hence, we focus on  $r \ll 1$  regions in the rest of this paper.

Note that the strongest LHC constraint to the parameter regions where the ATLAS diboson excess can be explained comes from the hadronic channel of  $\sigma(pp \rightarrow V' \rightarrow Vh)$  [42], e.g.  $\sigma(pp \rightarrow V' \rightarrow Vh) \lesssim 7$  fb for  $m_{Z'} = 2$  TeV. This implies  $\sigma(pp \rightarrow V' \rightarrow VV) < 7$  fb as we discussed in Sec. 3.1. If the coupling ratio  $\kappa_Z$  deviates from 1, this LHC bound becomes weaker, because the relation between  $\sigma(pp \rightarrow V' \rightarrow VV)$  and  $\sigma(pp \rightarrow V' \rightarrow Vh)$  are modified. However, in this model  $\kappa_Z$  is severely constrained close to 1 in the  $m_A \gg m_h$  regime (see Appendix A).

We show  $\sigma(pp \rightarrow V' \rightarrow VV)$  in Fig. 8, for  $m_{Z'} = 1.9, 2.0$ , and 2.1 TeV. We take  $\kappa_F = 1.00$ , and all heavy scalar masses to be the same as  $m_{Z'}$ ,  $m_{Z'} = m_A = m_{H'} = m_H$ . The color filled regions are excluded or constrained. The color notation is given in the caption. We find that the cross section is sensitive to the mass. For example, by changing  $m_{Z'}$  from 1.9 to 2 TeV (5 % mass difference), the cross section is decreased by about

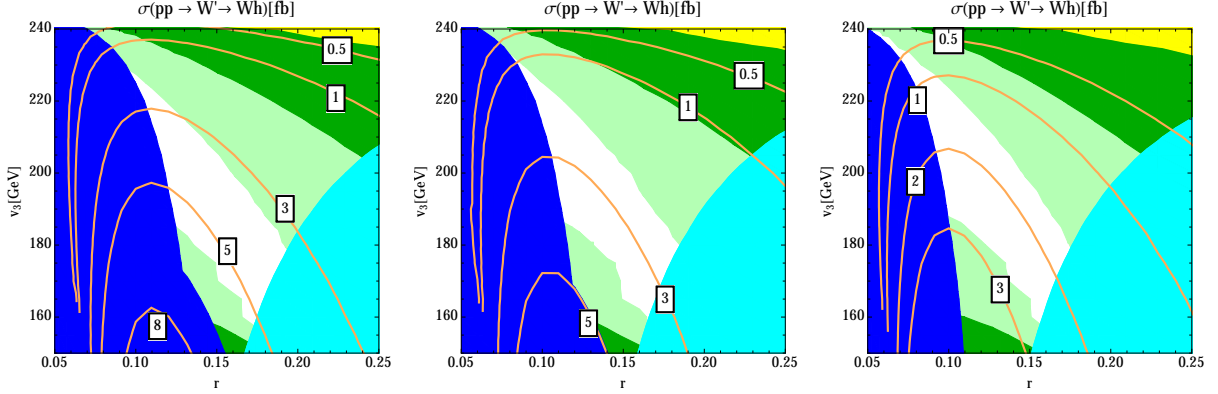


Figure 9. The cross sections of the diboson channels with  $h$ . We take  $m_{W'} \simeq 1.9$  TeV (the left panel), 2.0 TeV (the middle panel), and 2.1 TeV (the right panel). The colored regions are experimental and theoretical constraints.

40 %. This is because the PDF rapidly changes in the heavier mass regions (see Fig. 2).

Below the thick orange line the cross section  $\sigma(pp \rightarrow V' \rightarrow VV)$  is consistent with the ATLAS result. Here we apply the event selection efficiencies for the extended gauge model (cf. 10–16 % at  $m_{JJ} = 2$  TeV) [1]. Note that a part of these regions are constrained from the stability condition at  $\Lambda = 100$  TeV filled with light green. However, once we take account of the higher order correction, these constraint would be weaker as we discussed in Sec. 3.2.1. In the parameter regions shown in the figure,  $\sigma(pp \rightarrow W' \rightarrow WZ)/\sigma(pp \rightarrow Z' \rightarrow WW) \simeq 2$ . This is because the custodial symmetry is enhanced in the small  $r$  regime.

In the figure we show the leading order (LO) production cross sections. Next-to-leading order and next-to-leading logarithmic (NLO+NLL) corrections to the production cross sections of  $W'$  and  $Z'$  are evaluated in Ref [47, 48], and the  $K$ -factor ( $\sigma/\sigma_{\text{LO}}$ ) is about 1.3. This means that once we consider the QCD corrections, the production cross sections in the figures should be scaled by about 30 %, and the LHC bounds become severer, while the theoretical constraints do not change. After taking account of the  $K$ -factor, the LHC diboson excess can be explained for the regions below dashed orange lines, and the regions below the dashed blue lines are excluded by the LHC bounds.

Figure 9 shows  $\sigma(pp \rightarrow W' \rightarrow Wh)$ .<sup>#4</sup> The parameter choices and the color notations are the same as Fig. 8. We find that  $\sigma(pp \rightarrow W' \rightarrow Wh)/\sigma(pp \rightarrow Z' \rightarrow Zh) \simeq 2$  due to the enhancement of the custodial symmetry. We find  $\sigma(pp \rightarrow W' \rightarrow Wh) \times 20 \text{ fb}^{-1} \times \text{Br}(h \rightarrow b\bar{b}) \text{ Br}(W \rightarrow e\nu + \mu\nu) \sim 9$  events with  $\sigma \sim 4 \text{ fb}$  in the regions where the ATLAS diboson excess can be explained. This is consistent with the excess of the event for the 1.8–1.9 TeV bins at the CMS with a local significance of  $2.2\sigma$  for  $W' \rightarrow Wh \rightarrow \ell\nu b\bar{b}$  search [41], although the detail of the event selection has not been reported.

<sup>#4</sup>Detailed studies of this process are found in Refs. [49, 50].

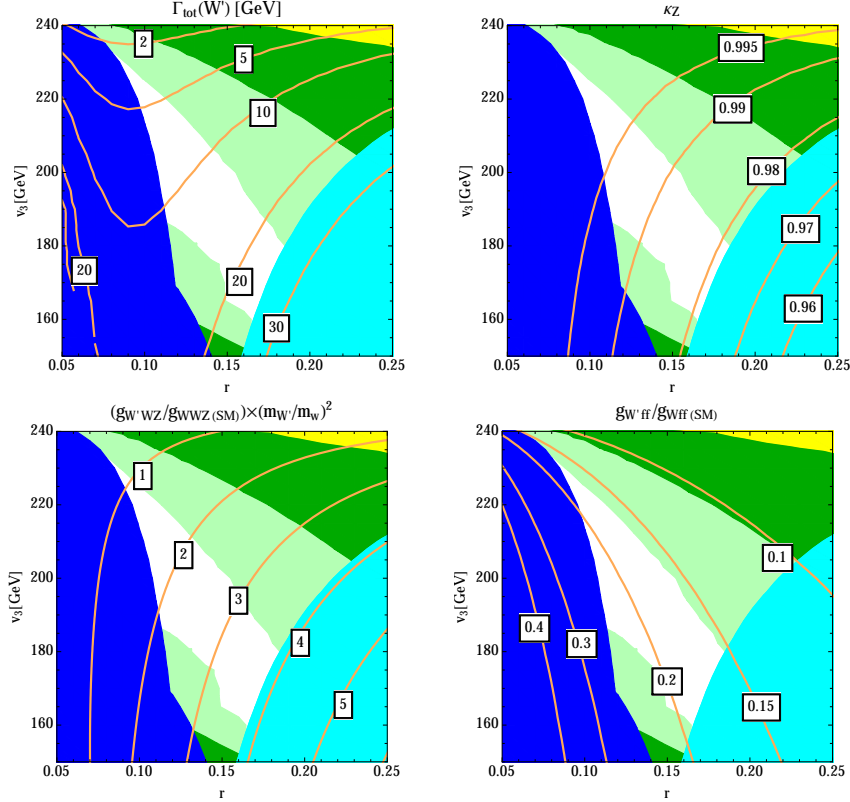


Figure 10.  $\Gamma_{\text{tot}}(W')$ ,  $\kappa_Z$ ,  $(g_{W'WZ}/g_{WWZ}^{\text{SM}}) \times (m_W/m_{W'})^2$ , and  $g_{W'ff}/g_{Wff}^{\text{SM}}$  for  $m_{Z'} = 2$  TeV. They are insensitive to small difference of  $m_{Z'}$ . The color notations are the same as in Fig. 8.

We show  $\Gamma_{\text{tot}}(W')$ ,  $\kappa_Z$ ,  $(g_{W'WZ}/g_{WWZ}^{\text{SM}}) \times (m_W/m_{W'})^2$  and  $g_{W'ff}/g_{Wff}^{\text{SM}}$  in Fig. 10. We fix  $m_{Z'} = 2$  TeV because they are not sensitive to the  $Z'$  mass. The choices of other parameters and the color notations are the same as in Fig. 8. The width of  $W'$  is shown in the top-left panel in the figure. We find that it is narrow and is less than 1 % of its mass, because the  $W'$  couplings to the SM particles are suppressed by powers of  $m_W/m_{W'}$  and the decay into the heavy scalars are suppressed kinematically. The observable related to the Higgs couplings  $\kappa_Z$  defined in Eq. (28) is shown in the top-right panels. The deviation from the SM prediction is small and the model is consistent with the current LHC data [51, 52]. Since the International Linear Collider (ILC) can measure the  $\kappa_Z$  at 1% level [53], some parameter points are within the reach of the proposed ILC. We show  $g_{W'WZ}/g_{WWZ}^{\text{SM}}$  and  $g_{W'ff}/g_{Wff}^{\text{SM}}$  at the lower panels in the figure. In the benchmark model used in Ref. [1],  $g_{W'WZ}/g_{WWZ}^{\text{SM}} = m_W^2/m_{W'}^2$  and  $g_{W'ff}/g_{Wff}^{\text{SM}} = 1$ . In our model, we find, due to the extra suppression by  $\sqrt{1 - v_3^2/v^2}$  and small  $r$ ,  $g_{W'WZ}/g_{WWZ}^{\text{SM}}$  is numerically the same order as the benchmark model although its  $m_{W'}$  dependence is  $m_W/m_{W'}$  (see Eq. (27)). On the other hand,  $g_{W'ff}/g_{Wff}^{\text{SM}}$  is about 10% of the benchmark model.

## 4 MC simulation of $W' \rightarrow WZ$ at $\sqrt{s} = 13$ TeV

In this section, we perform a collider simulation of  $pp \rightarrow W' \rightarrow WZ$  at  $\sqrt{s} = 13$  TeV. To study a discovery potential, we generate both QCD dijet background and  $pp \rightarrow W' \rightarrow WZ$  signal events.

We generate  $1.73 \times 10^6$  QCD dijet events as the dominant background by using PYTHIA 8.205 [54] with the generation cut so that the parton-parton center of mass energy must exceed 1 TeV and  $p_T > 400$  GeV at  $\sqrt{s} = 13$  TeV. The tree level production cross section is 350 pb. Our sample therefore corresponds to roughly  $\int dt \mathcal{L} = 5 \text{ fb}^{-1}$ . We use the Tune 4C for fragmentation and hadronization [55]. We also generate  $10^4$  signal events ( $pp \rightarrow W'(W'^+ + W'^-) \rightarrow WZ$ ) for the mass between 1800 and 3200 GeV, and take  $\Gamma_{\text{tot}}(W')$  to be 25 GeV in the simulation. Note that the total width of  $W'$  is less than about 30 GeV in the allowed region of this model (see Fig. 10). We also generate the signal and background events at  $\sqrt{s} = 8$  TeV and compare them with the ATLAS plots [1].

The simple detector simulator DELPHES3 [56] is modified using FASTJET3 [57, 58] so that the mass drop and the grooming cuts used in the ATLAS study can be applied to the jets. We apply the cluster track matching algorithm of DELPHES3 so that information of tracks inside jets can be used, otherwise the default ATLAS card is used.

Reconstruction of boosted objects using jet substructure was originally proposed in Refs. [59, 60]. See recent developments in Refs. [61, 62]. In our simulation, we closely follow the ATLAS analysis. The Cambridge-Aachen algorithm with  $R = 1.2$  is used [63, 64] for the jet clustering. Then,  $p_{T_1} > 600$  GeV,  $p_{T_2} > 540$  GeV,  $(p_{T_1} - p_{T_2})/(p_{T_1} + p_{T_2}) < 0.15$ ,  $|y_1 - y_2| < 1.2$ ,  $|\eta_1| < 2$  and  $|\eta_2| < 2$  are required for the jets. In addition, we require  $E_{T_{\text{miss}}} < 350$  GeV, and veto events with isolated electrons and muons with  $p_T > 20$  GeV. For each jet, the pair of the subjets which satisfies the subjet momentum balance criteria  $\sqrt{y} > \sqrt{y_f} = 0.45$  are selected, where

$$\sqrt{y} = \min(p_{T_{j_1}}, p_{T_{j_2}}) \frac{\Delta R_{(j_1, j_2)}}{m_0}. \quad (54)$$

Here,  $p_{T_{j_1}}$  and  $p_{T_{j_2}}$  are the transverse momenta of subjets  $j_1$  and  $j_2$ ,  $\Delta R_{(j_1, j_2)}$  is the distance between the subjets  $j_1$  and  $j_2$ , and  $m_0$  is the mass of the parent jet. Then the constituents of the selected pair of subjets are filtered. Namely the constituents are clustered with the radius parameter  $R = 0.3$ , and up to the highest 3 jets are taken to calculate the groomed jet mass and momentum. We require  $|m_V - m_j| < 13$  GeV, where  $m_V$  is  $m_Z$  or  $m_W$ , and  $m_j$  is an invariant mass of the groomed jet. Finally, the number of charged-particle tracks which are associated with the jet is required to be  $n_{ch} < 30$ . In Fig. 11, we show the distribution in  $n_{ch}$  and  $m_j$  plane for the events with  $m_{jj} > 1500$  GeV where all the cuts except for  $n_{ch}$  and  $m_j$  are applied. The ATLAS signal regions are marked by squares. The figure shows very good separation between the signal and the background events.

To check our simulation, we compare the distributions of our  $\sqrt{s} = 8$  TeV samples

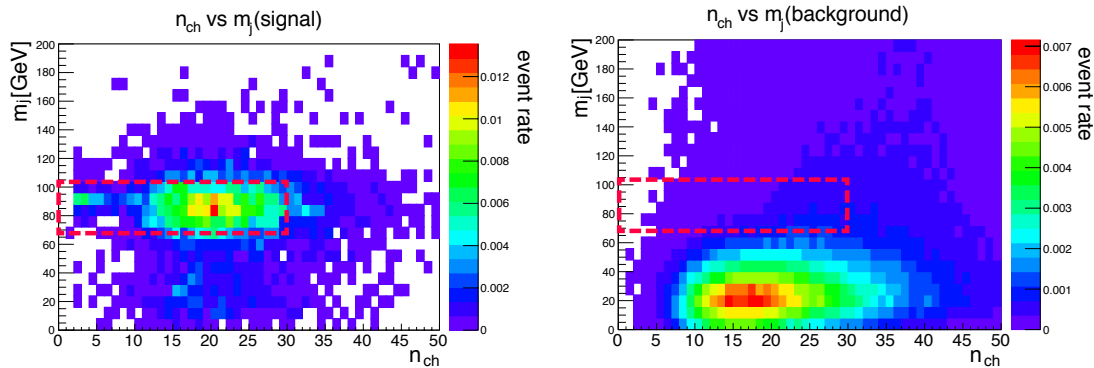


Figure 11. The distributions of the signal ( $m_{W'} = 1800$  GeV and  $\Gamma_{\text{tot}}(W') = 25$  GeV) and the dijet background in  $n_{\text{ch}}$  and  $m_j$  plane. All the cut except for  $n_{\text{ch}}$  and  $m_j$  are applied, and we required  $m_{jj} > 1500$  GeV. The ATLAS signal regions are marked by squares.

to the ATLAS ones. The Fig. 12 shows the reconstruction efficiency of the signal for various input  $W'$  mass. Our result at  $\sqrt{s} = 13$  TeV is also shown. We find that the signal selection efficiency agrees with the ATLAS one. Since the jets get narrower with increasing  $p_T$ , the signal efficiency becomes lower for higher  $W'$  mass.

On the other hand, we find that the number of the background events after all the selection cuts are twice as large as that of the ATLAS final result. The discrepancy in the total background events might arise from several sources. The number of charged tracks of QCD jets are controlled by soft physics and varies significantly depending on Monte Carlo (MC) generators and tunes of the parton shower parameters especially for gluon jets. The distributions are shown in the left panel of Fig. 13, under the cut of Fig. 1 of Ref. [1],  $1.62 \text{ TeV} < m_{jj} < 1.98 \text{ TeV}$  and  $60 \text{ GeV} < m_j < 110 \text{ GeV}$  together with the selection cuts listed above except that for  $n_{\text{ch}}$ , where  $m_{jj}$  is the dijet invariant mass. The signal distribution which is represented in the blue line agrees quite well with the ATLAS ones. However, the average number of charged tracks of dijet event is significantly higher than the ATLAS ones. To see the MC dependence, we also show the distribution of the MC sample generated by HERWIG++ with default tunes by the black line [65], which predicts slightly small  $\langle n_{\text{ch}} \rangle$  compared with PYTHIA8 Tune C4, but higher than ATLAS CT10 Tune.<sup>#5</sup>

In the right panel of Fig. 13, we also show the  $m_j$  distributions for the signal and background. The signal distribution agrees quite well with the ATLAS MC results again. For the background distribution, we find that the number of events above  $m_j > 50$  GeV is smaller compared with Fig. 1 of Ref. [1]. This is because we do not generate underlying events together with the dijet events.

In the experimental side, ATLAS counts the well reconstructed track inside the jet. The efficiencies are not implemented in our simulation. Naively speaking, the

<sup>#5</sup> In the study of quark-gluon separation [66], HERWIG++ reproduces high gluon  $p_T$  jet nature well.

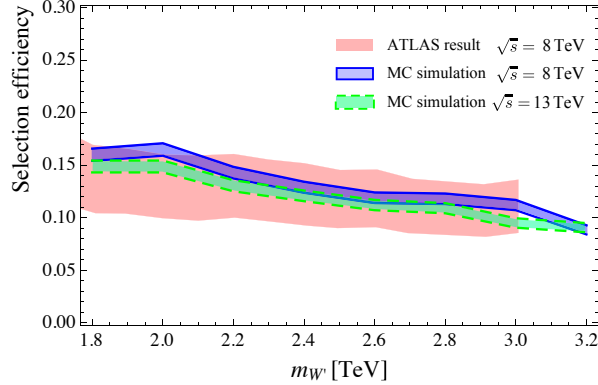


Figure 12. The event selection efficiencies for  $W' \rightarrow WZ \rightarrow JJ$  simulated events generated by PYTHIA 8 as a function of the  $W'$  mass at  $\sqrt{s} = 8$  and 13 TeV. The red band is the result of the ATLAS [1], where the thickness corresponds to  $\pm 1 \sigma$  statistical and systematical errors. Our result of MC simulation at  $\sqrt{s} = 8$  (13) TeV is represented in the blue (green) band where the thickness corresponds to  $\pm 1 \sigma$  statistical error.

efficiency is expected to be lower for the jets with high charged track multiplicity. For jet clustering, ATLAS selects calorimeter towers using Topocluster algorithm and does not use cluster-track matching which is only crudely implemented in our simulation. In any case, data driven approaches are adopted in Ref. [1] to estimate the selection efficiency, and reproducing the result precisely is beyond the scope of this paper. It is probably worth doing more dedicated theoretical and experimental studies on jet nature relevant to the boosted  $W$  and  $Z$  bosons reconstruction in future.

Keeping crudeness of our simulation in mind, we estimate the signal efficiency at  $\sqrt{s} = 13$  TeV using our signal MC and detector simulation without rescaling, while the number of the background events obtained from our MC is rescaled by factor of  $1/2$  which is needed to reproduce the ATLAS results at  $\sqrt{s} = 8$  TeV. The scaling approach comes from an assumption that the change in the center of mass energy from 8 TeV to 13 TeV does not alter the structure inside jets of the same  $p_T$  jets. Note that gluon jets are involved in the QCD background at  $\sqrt{s} = 13$  TeV but this effect is not taken into account. Under this assumption, the background is fitted to estimate the distribution, and the result is shown in the left panel of Fig. 14. We found 169 events/ $10 \text{ fb}^{-1}$  for  $1550 \text{ GeV} < m_{jj} < 3550 \text{ GeV}$  after rescaling. We also show the dijet invariant mass distributions of the signal for various input  $W'$  mass in the right panel of Fig. 14.

Figure 15 shows expected the exclusion limit at 95 % C.L. for  $\sigma(pp \rightarrow V' \rightarrow VV)$  at  $\sqrt{s} = 13$  TeV.<sup>#6</sup> We calculated  $\Delta\chi^2$  of the signal plus background distributions to the background distribution. For the signal, we generate  $10^4$  signal events to obtain the result for each  $m_{W'}$ , and take the number of events in the bins  $i_{\text{max}} - 3 \leq i \leq i_{\text{max}} + 3$ ,

<sup>#6</sup>Prospects for the electroweak gauge boson scattering which can also probe  $W'$  are discussed in, for example, Ref. [67].

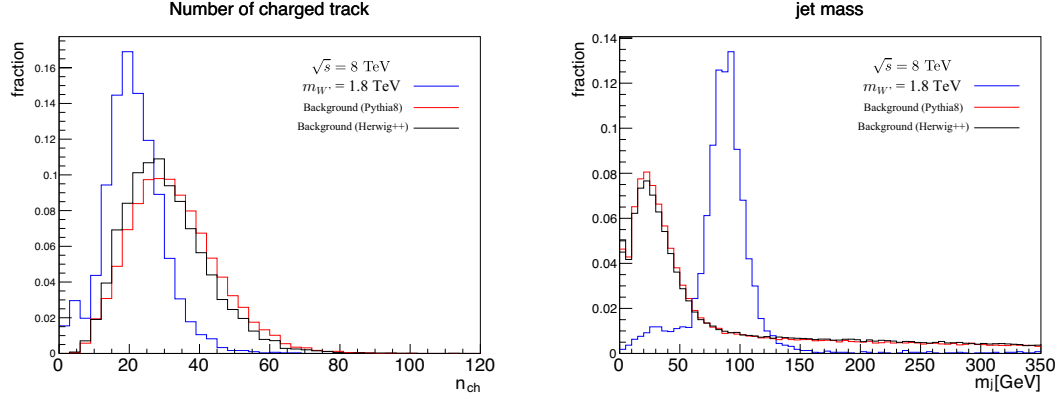


Figure 13. The distributions of the number of charged tracks  $n_{\text{ch}}$  (left) and the jet mass  $m_j$  (right) for the signal (Blue) and background events (Black and Red). We take  $m_{W'} = 1800$  GeV and  $\Gamma_{\text{tot}}(W') = 25$  GeV. We simulate the background events using PYTHIA8 (Red) and HERWIG++ (Black).

where  $i_{\text{max}}$  is the highest signal event bin and the bin size is 50 GeV. Then, we rescale them by the cross section and luminosity. The selection efficiency of the signal event is shown in Fig. 12. For the background, we use our fit and rescaled it by the luminosity. Here y-axis means  $\sigma(pp \rightarrow W' \rightarrow WZ) + \sigma(pp \rightarrow Z' \rightarrow WW)$  with the mass at  $m_{V'}$ . We find that the region where  $\sigma(pp \rightarrow V' \rightarrow VV)$  is larger than 20 fb may be excluded at  $\int dt\mathcal{L} = 10 \text{ fb}^{-1}$  and  $\sqrt{s} = 13$  TeV.

## 5 Future prospects: 13 TeV analyses

In this section, we analyze the future prospects of  $W'$  and  $Z'$  searches by applying result in Sec. 4.

We investigate the prospects for the  $\sqrt{s} = 13$  TeV collision in the case of  $m_{Z'} = 2$  TeV. In Fig. 16, we show contours of the several cross sections by orange dashed lines in  $r$ - $v_3$  planes:  $\sigma(pp \rightarrow W')\text{Br}(W' \rightarrow WZ) + \sigma(pp \rightarrow Z')\text{Br}(Z' \rightarrow WW)$ ,  $\sigma(pp \rightarrow W')\text{Br}(W' \rightarrow Wh)$ ,  $\sigma(pp \rightarrow W')\text{Br}(W' \rightarrow \ell\nu)$ ,  $\sigma(pp \rightarrow W')\text{Br}(W' \rightarrow jj) + \sigma(pp \rightarrow Z')\text{Br}(Z' \rightarrow jj)$ , and  $\sigma(pp \rightarrow Z')\text{Br}(Z' \rightarrow \ell\ell)$ . The color filled regions are excluded and constrained as we discussed in Sec. 3.3. The color notations are the same as in Fig. 8.

The expected exclusion limit at  $\sqrt{s} = 13$  TeV provided in Fig. 15 is shown by the red (dashed) line for  $\int dt\mathcal{L} = 10$  (100)  $\text{fb}^{-1}$ . The masses of  $W'$  and  $Z'$  are highly degenerate in the small  $r$  regime, and we assume that the signal efficiency for  $Z' \rightarrow WW$  event is equivalent to the one for  $W' \rightarrow WZ$  which is simulated in the previous section. Thus we can apply the prospect shown in Fig. 15 to  $\sigma(pp \rightarrow W' \rightarrow WZ) + \sigma(pp \rightarrow Z' \rightarrow WW)$ . The region where the ATLAS diboson excess can be explained is within the reach of the LHC at  $\int dt\mathcal{L} = 10 \text{ fb}^{-1}$  and  $\sqrt{s} = 13$  TeV. In addition, the cross sections of the other



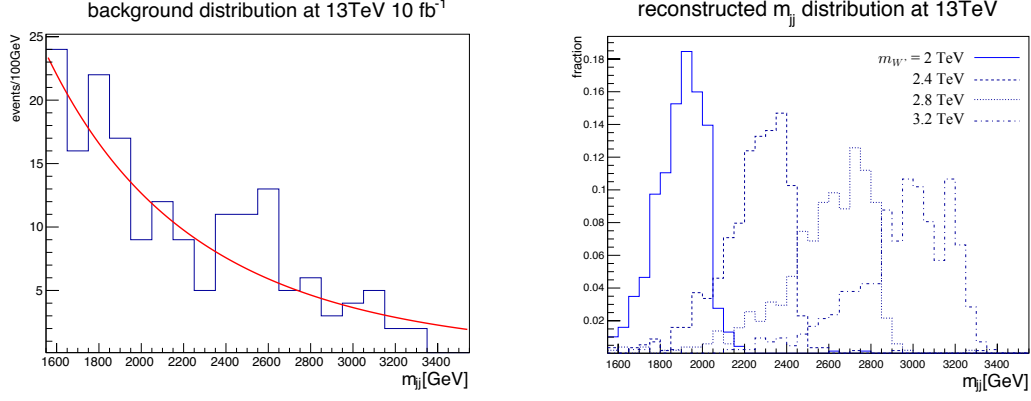


Figure 14. The  $m_{jj}$  distributions for the background (left) and the signal (right) at  $\sqrt{s} = 13$  TeV. The background distribution is for  $10 \text{ fb}^{-1}$ , and the signal distributions are normalized to be 1 for various input  $W'$  mass.

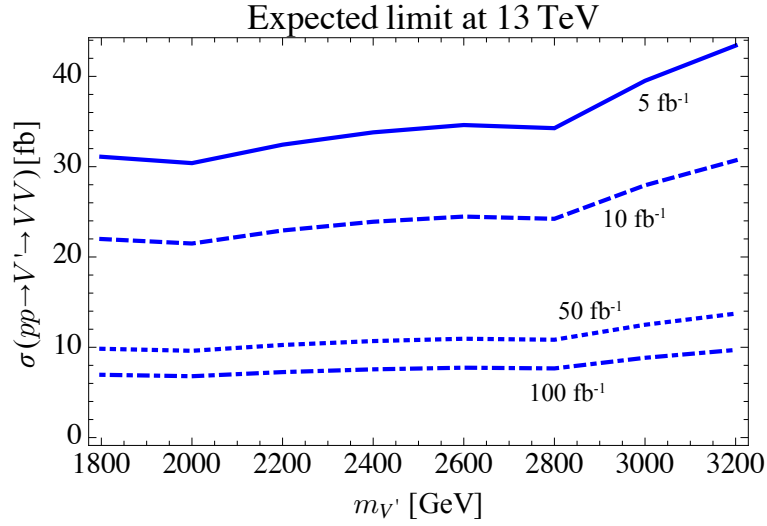


Figure 15. Expected limit on  $\sigma(pp \rightarrow V' \rightarrow VV)$  at  $\sqrt{s} = 13$  TeV. We take  $\Gamma_{\text{tot}}(V') = 25 \text{ GeV}$ .



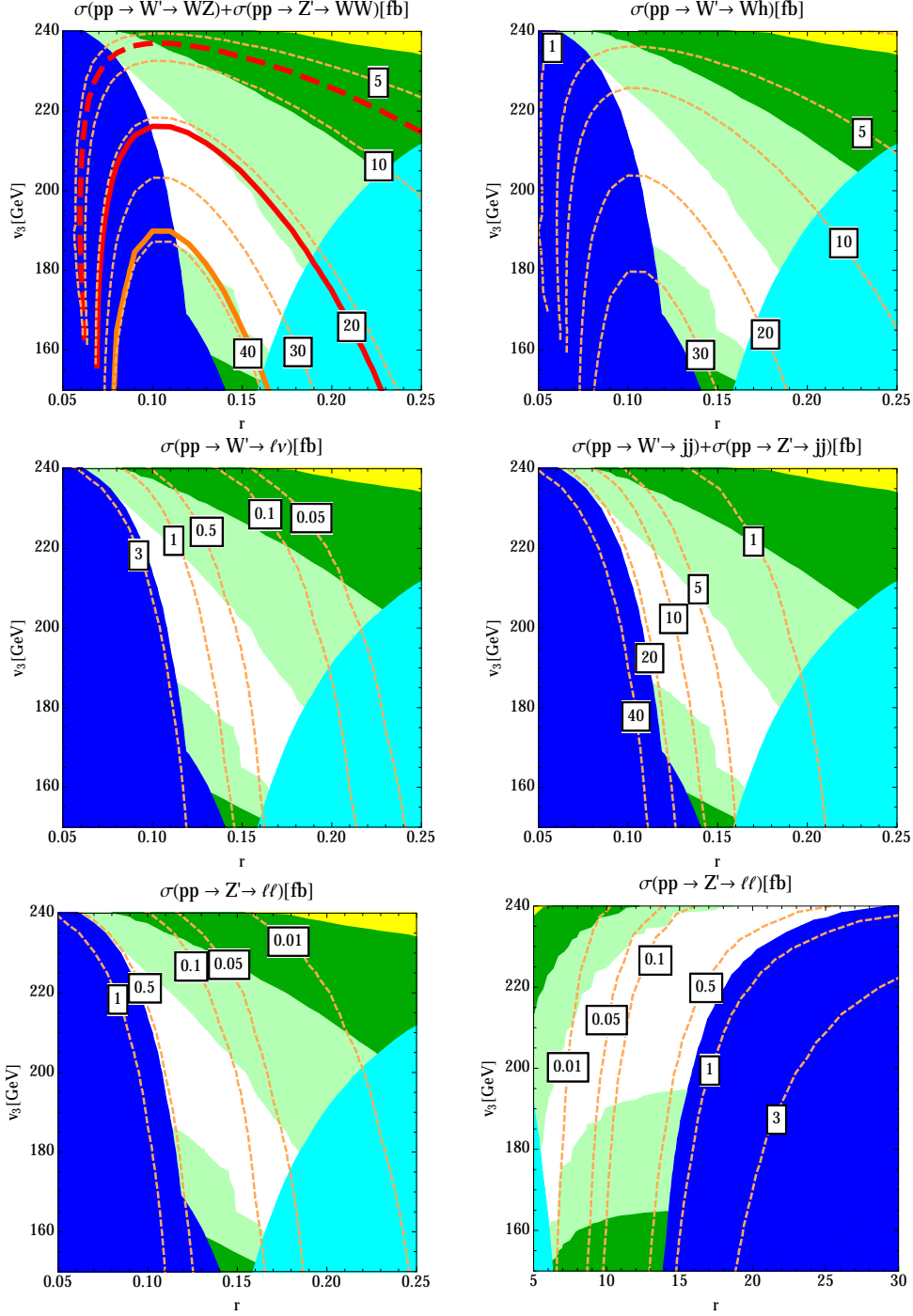


Figure 16. The prospects for the  $\sqrt{s} = 13$  TeV collision. We take  $m_{Z'} = m_A = m_{H'} = m_H = 2000$  GeV,  $\kappa_F = 1.00$ . The color notation is the same as in Fig. 8. Below the thick orange line, the cross section  $\sigma(pp \rightarrow V' \rightarrow VV)$  is enough to explain the diboson excess at ATLAS. Below the (dashed) red line is expected to be excluded with  $\int dt \mathcal{L} = 10$  (100)  $\text{fb}^{-1}$ .

channels are also large, so that the spin-1 resonances could be probed in the channels as well.

We plot the  $\sqrt{s} = 13$  TeV cross sections as a function of spin-1 resonance mass in Fig. 17. We take the universal mass  $m_{Z'} = m_A = m_{H'} = m_H$ ,  $v_3 = 200$  GeV, and  $\kappa_F = 1.00$  in Fig. 17. The color notation is the same as in Fig. 8. The mass of  $W'$  is highly degenerate with the mass of  $Z'$  in this figure. We find that the spin-1 resonances lighter than 2.1 (2.6) TeV can be excluded by the diboson search at the LHC with  $\int dt \mathcal{L} = 10$  (100)  $\text{fb}^{-1}$ . Figure 18 shows the same cross sections for another parameter set ( $v_3 = 150$  GeV and  $\kappa_F = 0.99$ ). With the consideration of the bounded below condition, we find that the spin-1 resonances up to masses of 2.3 (2.6) TeV can be excluded with  $\int dt \mathcal{L} = 10$  (100)  $\text{fb}^{-1}$ .

Before closing this section, we briefly comment on the prospect for the large  $r$  region. Under the several theoretical bounds, this model has two allowed regions, namely small  $r$  and large  $r$  regions (see Fig. 5). The cross section of  $pp \rightarrow Z' \rightarrow \ell\ell$  is enhanced by  $r^2$  factor in large  $r$  regime (see Eq. (72)). ATLAS study found  $m_{Z'}$  around 3 TeV with the cross section around 0.01 fb is accessible with the high luminosity LHC at  $\sqrt{s} = 14$  TeV with integrated luminosity 3000  $\text{fb}^{-1}$  [68]. Thus we can expect that the cross section for the large  $r$  region in the model is accessible at the LHC Run-2 as we can see in Fig. 16. However, the  $r$  regime would be constrained from the electroweak precision parameters at one-loop level due to the custodial symmetry breaking.

## 6 Conclusion

Motivated by the ATLAS diboson excess around 2 TeV, we have investigated the phenomenology of the spin-1 resonances ( $W'$  and  $Z'$ ) in the partially composite standard model. In this model,  $W'$  and  $Z'$  couple to the SM fermions weakly through the mixing to the elementary gauge bosons. We find that the main decay modes of the resonances are  $V' \rightarrow VV$  and  $V' \rightarrow Vh$ , and the width is narrow enough so that the ATLAS diboson excess can be explained. The couplings of the spin-1 resonances with the SM sector can be controlled by the ratio of the Higgs VEVs so that the ATLAS diboson excess can be explained.

We have explored not only the current bounds from the LHC and the precision measurements but also the theoretical constraints, i.e. perturbativity condition, bounded below condition, global minimum vacuum condition, and stability condition of the scalar potential. The parameter regions where the diboson excess at the ATLAS can be explained are still allowed after including those constraints.

In order to investigate future prospects of the spin-1 resonance search, we have performed the simulation at  $\sqrt{s} = 13$  TeV LHC, and estimated model independent exclusion limit for  $\sigma(pp \rightarrow V' \rightarrow VV \rightarrow JJ)$  shown in Fig. 15. Applying our simulation result, we find that the parameter regions consistent with the ATLAS diboson excess will be excluded at  $\int dt \mathcal{L} = 10$   $\text{fb}^{-1}$  and  $\sqrt{s} = 13$  TeV.

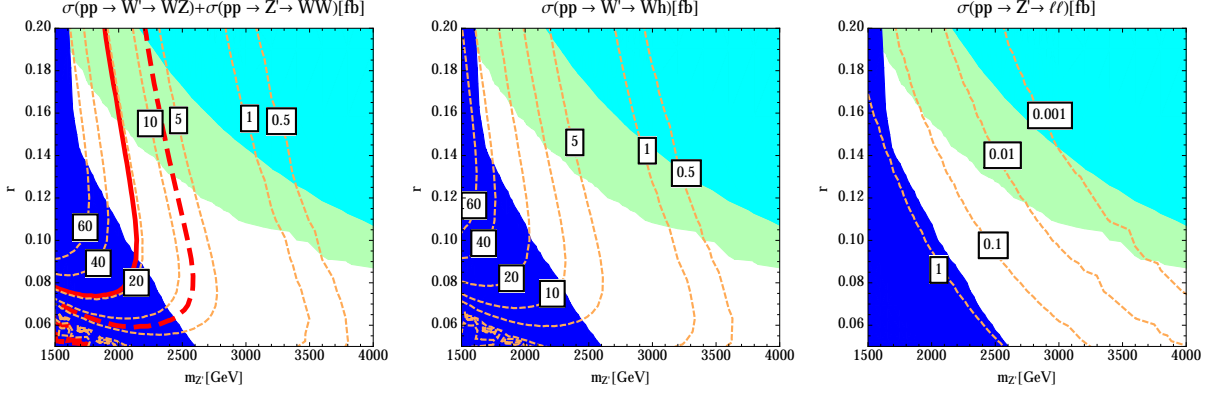


Figure 17. The prospects of the discovery as a function of  $m_{Z'}$  and  $r$  for the LHC Run-2. We take  $v_3 = 200$  GeV and  $\kappa_F = 1.00$ . The color notation is the same as in Fig. 8. The (dashed) red is the future expected exclusion limit for  $\int dt \mathcal{L} = 10$  (100)  $\text{fb}^{-1}$ .

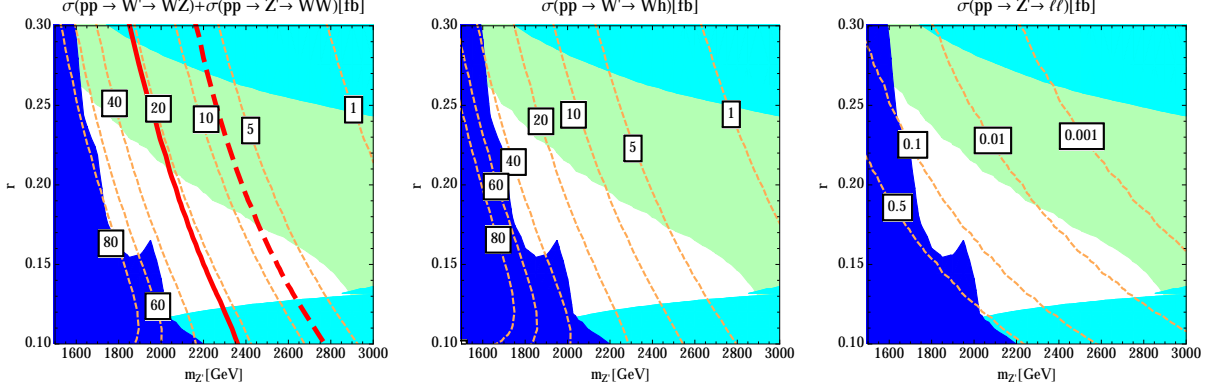


Figure 18. The prospects of the discovery as a function of  $m_{Z'}$  and  $r$  for the LHC Run-2. We take  $v_3 = 150$  GeV and  $\kappa_F = 0.99$ . Below the (dashed) red line is expected to be excluded with  $\int dt \mathcal{L} = 10$  (100)  $\text{fb}^{-1}$ .

Finally, we have investigated future prospects of diboson resonance search in our model. The spin-1 resonances up to a mass of 2.6 TeV can be probed at  $\sqrt{s} = 13$  TeV and  $\int dt \mathcal{L} = 100 \text{ fb}^{-1}$ .

## Acknowledgments

The authors would like to thank Koji Terashi and Ryuichiro Kitano for useful discussions. This work is supported by JSPS KAKENHI No. 26287039 (M.M.N.). The work is supported by Grant-in-Aid for Scientific research from the Ministry of Education, Science, Sports, and Culture (MEXT), Japan, No. 23104006 (T.A. and M.M.N.) and No. 25105011 (T.K.), and also by World Premier International Research Center Initiative (WPI Initiative), MEXT, Japan.

## A Viable range of the coupling ratio $\kappa_Z$

In this appendix, we show  $\kappa_Z$  is very restricted to be one. We first replace the Higgs quartic couplings  $\lambda_i$  by the other parameters Eq. (34). Here we take  $m_A = m_{H'} = m_H$  for simplicity, and work in  $m_A \gg m_h$  regime. For  $r \ll 1$  regime, we find

$$\lambda_1 \simeq 0, \quad (55)$$

$$\lambda_2 \simeq f_1(\kappa_F, \kappa_Z), \quad (56)$$

$$\lambda_3 \simeq \frac{m_h^2}{2v^2} \kappa_F^2 + \frac{m_A^2}{2v^2} (1 - \kappa_F^2), \quad (57)$$

$$\lambda_{12} \simeq 0, \quad (58)$$

$$\lambda_{23} \simeq f_2(\kappa_F, \kappa_Z), \quad (59)$$

$$\lambda_{31} \simeq 0, \quad (60)$$

and for  $r \gg 1$  regime,

$$\lambda_1 \simeq f_1(\kappa_F, \kappa_Z), \quad (61)$$

$$\lambda_2 \simeq 0, \quad (62)$$

$$\lambda_3 \simeq \frac{m_h^2}{2v^2} \kappa_F^2 + \frac{m_A^2}{2v^2} (1 - \kappa_F^2), \quad (63)$$

$$\lambda_{12} \simeq 0, \quad (64)$$

$$\lambda_{23} \simeq 0, \quad (65)$$

$$\lambda_{31} \simeq f_2(\kappa_F, \kappa_Z), \quad (66)$$

$$(67)$$

where

$$f_1(\kappa_F, \kappa_Z) \simeq \frac{m_h^2}{2v^2} - (1 - \kappa_F) \frac{v_3^2}{v^2} \frac{2(m_A^2 - m_h^2)}{v^2 - v_3^2} + (1 - \kappa_Z) \frac{m_A^2 - m_h^2}{v^2 - v_3^2}, \quad (68)$$

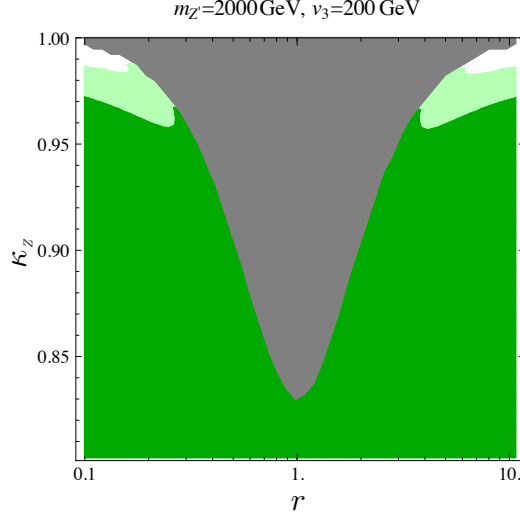


Figure 19. The viable range of the coupling ratio  $\kappa_Z$ , where we take  $v_3 = 200$  GeV,  $m_{Z'} = m_A = m_{H'} = m_H = 2$  TeV, and  $\kappa_F = 1.00$ . The regions where  $\lambda_i(\mu = 10$  (100) TeV)  $> (4\pi)^2$  are filled with green (light green).

$$f_2(\kappa_F, \kappa_Z) \simeq \frac{m_h^2}{v^2} + (1 - \kappa_F) \frac{v^2 - 3v_3^2}{v^2} \frac{m_A^2 - m_h^2}{v^2 - v_3^2} + (1 - \kappa_Z) \frac{m_A^2 - m_h^2}{v^2 - v_3^2}. \quad (69)$$

In Eqs. (68) and (69), we make an expansion around  $\kappa_F \simeq 1$  and  $\kappa_Z \simeq 1$ . Since both coefficients of  $(1 - \kappa_F)$  and  $(1 - \kappa_Z)$  are large enough in  $m_A \gg v$  regime, even the small deviations of  $\kappa_F$  and  $\kappa_Z$  from 1 change the Higgs quartic couplings  $\lambda_i$  drastically.

Let us consider the case of  $\kappa_F = 1$ . The largest Higgs quartic coupling is  $\lambda_{23}$  ( $\lambda_{31}$ ) in the  $r \ll 1$  ( $r \gg 1$ ) regime. We further demand  $\lambda_{23}$  ( $\lambda_{31}$ )  $< (4\pi)^2$ , namely

$$\kappa_Z > 1 - \frac{(16\pi^2 v^2 - m_h^2)}{(m_A^2 - m_h^2)} \left( 1 - \frac{v_3^2}{v^2} \right). \quad (70)$$

Due to the running effects, these quartic couplings can be even larger at the high scale, so that the lower bound on  $\kappa_Z$  is actually severer than above estimation.

In Fig. 19, we show that the viable range of the coupling ratio  $\kappa_Z$ , where we take  $v_3 = 200$  GeV,  $m_{Z'} = m_A = m_{H'} = m_H = 2$  TeV, and  $\kappa_F = 1.00$ . The regions where  $\lambda_i(\mu = 10$  (100) TeV)  $> (4\pi)^2$  are filled with green (light green), and there is no physical solution in the gray region. The maximal value of  $\kappa_Z$  is achieved at a boundary of the gray region. The white area represents the allowed region of parameter space. Thus we find  $\kappa_Z$  is severely constrained close to its maximized value for  $m_A \gg m_h$ .

## B Production cross sections of $W'$ and $Z'$

The leading order production cross sections of  $W'$  and  $Z'$  are given as follows.

$$\begin{aligned}\sigma(pp \rightarrow W'^{\pm} X) &\simeq \frac{\pi}{12s} \frac{m_W^2}{m_{W'}^2} \frac{e^2}{s_W^2} \frac{1}{r^2} \left(1 - \frac{v_3^2}{v^2}\right) \int_{m_{W'}/s}^1 \frac{dx}{x} \\ &\times \left( f_u(x, m_{W'}) f_{\bar{d}}\left(\frac{m_{W'}^2}{sx}, m_{W'}\right) + f_{\bar{d}}(x, m_{W'}) f_u\left(\frac{m_{W'}^2}{sx}, m_{W'}\right) \right. \\ &\quad + f_d(x, m_{W'}) f_{\bar{u}}\left(\frac{m_{W'}^2}{sx}, m_{W'}\right) + f_{\bar{u}}(x, m_{W'}) f_d\left(\frac{m_{W'}^2}{sx}, m_{W'}\right) \\ &\quad \left. + (u \leftrightarrow c, d \leftrightarrow s) \right),\end{aligned}\tag{71}$$

$$\begin{aligned}\sigma(pp \rightarrow Z' X) &\simeq \frac{\pi}{6s} \frac{m_W^2}{m_{W'}^2} \frac{e^2}{s_W^2} \frac{1}{r^2} \left(1 - \frac{v_3^2}{v^2}\right) \\ &\times \left( \left( \left(1 - r^2 \frac{s_Z^2}{c_Z^2}\right) T_f^3 + r^2 \frac{s_Z^2}{c_Z^2} Q_f \right)^2 + \left( r^2 \frac{s_Z^2}{c_Z^2} Q_f \right)^2 \right) \int_{m_{Z'}/s}^1 \frac{dx}{x} \\ &\times \left( f_u(x, m_{Z'}) f_{\bar{u}}\left(\frac{m_{Z'}^2}{sx}, m_{Z'}\right) + f_{\bar{u}}(x, m_{Z'}) f_u\left(\frac{m_{Z'}^2}{sx}, m_{Z'}\right) \right. \\ &\quad \left. + (u \leftrightarrow d, s, c, b) \right),\end{aligned}\tag{72}$$

where  $s$  is a square of the center of mass energy of the  $pp$  collider and  $f_q(x, Q)$  is the parton distributions inside the  $p$  at the factorization scale  $Q$  for quark flavor  $q$ . Note that Eq. (71) is a sum of production cross section of  $W'^+$  and  $W'^-$ .

## C Renormalization group equations

We derive the one-loop  $\beta$  functions for this model [69, 70], and obtain,

$$\beta_{g_0} = -3g_0^3,\tag{73}$$

$$\beta_{g_1} = -7g_1^3,\tag{74}$$

$$\beta_{g_2} = 7g_2^3,\tag{75}$$

$$\beta_{g_s} = -7g_s^3,\tag{76}$$

$$\beta_{\lambda_1} = 24\lambda_1^2 + 2\lambda_{12}^2 + 2\lambda_{31}^2 - 9\lambda_1(g_0^2 + g_1^2) + \frac{9}{8}g_0^4 + \frac{9}{8}g_1^4 + \frac{9}{4}g_0^2g_1^2,\tag{77}$$

$$\beta_{\lambda_2} = 24\lambda_2^2 + 2\lambda_{12}^2 + 2\lambda_{23}^2 - 3\lambda_2(3g_1^2 + g_2^2) + \frac{9}{8}g_1^4 + \frac{3}{8}g_2^4 + \frac{3}{4}g_1^2g_2^2,\tag{78}$$

$$\begin{aligned}\beta_{\lambda_3} &= 24\lambda_3^2 + 2\lambda_{23}^2 + 2\lambda_{31}^2 - 3\lambda_3(3g_0^2 + g_2^2) + \frac{9}{8}g_0^4 + \frac{3}{8}g_2^4 + \frac{3}{4}g_0^2g_2^2 \\ &\quad + 2\lambda_3(3y_t^2 + 3y_b^2 + y_\tau^2) - \frac{3}{2}y_t^4 - \frac{3}{2}y_b^4 - \frac{1}{2}y_\tau^4,\end{aligned}\tag{79}$$

$$\beta_{\lambda_{12}} = 4\lambda_{12}^2 + 12\lambda_{12}(\lambda_1 + \lambda_2) + 4\lambda_{23}\lambda_{31} - \frac{3}{2}\lambda_{12}(3g_0^2 + 6g_1^2 + g_2^2) + \frac{9}{4}g_1^4, \quad (80)$$

$$\begin{aligned} \beta_{\lambda_{23}} = & 4\lambda_{23}^2 + 12\lambda_{23}(\lambda_2 + \lambda_3) + 4\lambda_{12}\lambda_{31} - \frac{3}{2}\lambda_{23}(3g_0^2 + 3g_1^2 + 2g_2^2) + \frac{3}{4}g_2^4 \\ & + \lambda_{23}(3y_t^2 + 3y_b^2 + y_\tau^2), \end{aligned} \quad (81)$$

$$\begin{aligned} \beta_{\lambda_{31}} = & 4\lambda_{31}^2 + 12\lambda_{31}(\lambda_1 + \lambda_3) + 4\lambda_{12}\lambda_{23} - \frac{3}{2}\lambda_{31}(6g_0^2 + 3g_1^2 + g_2^2) + \frac{9}{4}g_0^4 \\ & + \lambda_{31}(3y_t^2 + 3y_b^2 + y_\tau^2), \end{aligned} \quad (82)$$

$$\beta_{y_t} = y_t \left( -\frac{9}{4}g_0^2 - \frac{17}{12}g_2^2 - 8g_s^2 + \frac{9}{4}y_t^2 + \frac{3}{4}y_b^2 + \frac{1}{2}y_\tau^2 \right), \quad (83)$$

$$\beta_{y_b} = y_b \left( -\frac{9}{4}g_0^2 - \frac{5}{12}g_2^2 - 8g_s^2 + \frac{3}{4}y_t^2 + \frac{9}{4}y_b^2 + \frac{1}{2}y_\tau^2 \right), \quad (84)$$

$$\beta_{y_\tau} = y_\tau \left( -\frac{9}{4}g_0^2 - \frac{15}{4}g_2^2 + \frac{3}{2}y_t^2 + \frac{3}{2}y_b^2 + \frac{5}{4}y_\tau^2 \right), \quad (85)$$

where  $\beta$  functions are defined in the following notation,

$$\frac{d(\text{coupling})}{d\ln\mu} = \frac{\beta_{(\text{coupling})}}{(4\pi)^2}. \quad (86)$$

## References

- [1] G. Aad *et al.* [ATLAS Collaboration], arXiv:1506.00962 [hep-ex].
- [2] V. Khachatryan *et al.* [CMS Collaboration], JHEP **1408**, 173 (2014) [arXiv:1405.1994 [hep-ex]],
- [3] H. S. Fukano, M. Kurachi, S. Matsuzaki, K. Terashi and K. Yamawaki, arXiv:1506.03751 [hep-ph].
- [4] J. Hisano, N. Nagata and Y. Omura, arXiv:1506.03931 [hep-ph].
- [5] D. B. Franzosi, M. T. Frandsen and F. Sannino, arXiv:1506.04392 [hep-ph].
- [6] S. S. Xue, arXiv:1506.05994 [hep-ph].
- [7] K. Cheung, W. Y. Keung, P. Y. Tseng and T. C. Yuan, arXiv:1506.06064 [hep-ph].
- [8] B. A. Dobrescu and Z. Liu, arXiv:1506.06736 [hep-ph].
- [9] J. A. Aguilar-Saavedra, arXiv:1506.06739 [hep-ph].
- [10] A. Alves, A. Berlin, S. Profumo and F. S. Queiroz, arXiv:1506.06767 [hep-ph].

- [11] Y. Gao, T. Ghosh, K. Sinha and J. H. Yu, arXiv:1506.07511 [hep-ph].
- [12] A. Thamm, R. Torre and A. Wulzer, arXiv:1506.08688 [hep-ph].
- [13] J. Brehmer, J. Hewett, J. Kopp, T. Rizzo and J. Tattersall, arXiv:1507.00013 [hep-ph].
- [14] Q. H. Cao, B. Yan and D. M. Zhang, arXiv:1507.00268 [hep-ph].
- [15] G. Cacciapaglia and M. T. Frandsen, arXiv:1507.00900 [hep-ph].
- [16] T. Abe, R. Nagai, S. Okawa and M. Tanabashi, arXiv:1507.01185 [hep-ph].
- [17] B. A. Dobrescu and Z. Liu, arXiv:1507.01923 [hep-ph].
- [18] P. Coloma, B. A. Dobrescu and J. Lopez-Pavon, arXiv:1508.04129 [hep-ph].
- [19] K. Agashe, R. Contino and A. Pomarol, Nucl. Phys. B **719**, 165 (2005) [hep-ph/0412089].
- [20] G. Panico and A. Wulzer, JHEP **1109**, 135 (2011) [arXiv:1106.2719 [hep-ph]].
- [21] R. Contino, D. Marzocca, D. Pappadopulo and R. Rattazzi, JHEP **1110**, 081 (2011) [arXiv:1109.1570 [hep-ph]].
- [22] B. Bellazzini, C. Csaki, J. Hubisz, J. Serra and J. Terning, JHEP **1211**, 003 (2012) [arXiv:1205.4032 [hep-ph]].
- [23] T. Abe and R. Kitano, Phys. Rev. D **88**, no. 1, 015019 (2013) [arXiv:1305.2047 [hep-ph]].
- [24] M. Bando, T. Fujiwara and K. Yamawaki, Prog. Theor. Phys. **79**, 1140 (1988).
- [25] M. Bando, T. Kugo, S. Uehara, K. Yamawaki and T. Yanagida, Phys. Rev. Lett. **54**, 1215 (1985).
- [26] M. Bando, T. Kugo and K. Yamawaki, Prog. Theor. Phys. **73**, 1541 (1985).
- [27] M. Bando, T. Kugo and K. Yamawaki, Nucl. Phys. B **259**, 493 (1985).
- [28] H. Georgi, Nucl. Phys. B **266**, 274 (1986).
- [29] C. Quigg, Front. Phys. **56**, 1 (1983).
- [30] E. Eichten, I. Hinchliffe, K. D. Lane and C. Quigg, Rev. Mod. Phys. **56**, 579 (1984) [Rev. Mod. Phys. **58**, 1065 (1986)].
- [31] G. Altarelli, B. Mele and M. Ruiz-Altaba, Z. Phys. C **45**, 109 (1989) [Z. Phys. C **47**, 676 (1990)].



- [32] J. Pumplin, D. R. Stump, J. Huston, H. L. Lai, P. M. Nadolsky and W. K. Tung, JHEP **0207**, 012 (2002) [hep-ph/0201195].
- [33] G. Degrandi, S. Di Vita, J. Elias-Miro, J. R. Espinosa, G. F. Giudice, G. Isidori and A. Strumia, JHEP **1208**, 098 (2012) [arXiv:1205.6497 [hep-ph]].
- [34] M. F. Zoller, arXiv:1411.2843 [hep-ph].
- [35] G. Aad *et al.* [ATLAS Collaboration], JHEP **1409**, 037 (2014) [arXiv:1407.7494 [hep-ex]].
- [36] V. Khachatryan *et al.* [CMS Collaboration], Phys. Rev. D **91**, no. 9, 092005 (2015) [arXiv:1408.2745 [hep-ex]].
- [37] G. Aad *et al.* [ATLAS Collaboration], Phys. Rev. D **90**, no. 5, 052005 (2014) [arXiv:1405.4123 [hep-ex]].
- [38] V. Khachatryan *et al.* [CMS Collaboration], JHEP **1504**, 025 (2015) [arXiv:1412.6302 [hep-ex]].
- [39] V. Khachatryan *et al.* [CMS Collaboration], arXiv:1502.04994 [hep-ex].
- [40] G. Aad *et al.* [ATLAS Collaboration], arXiv:1503.08089 [hep-ex].
- [41] CMS Collaboration [CMS Collaboration], CMS-PAS-EXO-14-010.
- [42] V. Khachatryan *et al.* [CMS Collaboration], arXiv:1506.01443 [hep-ex].
- [43] G. Aad *et al.* [ATLAS Collaboration], Eur. Phys. J. C **75**, no. 2, 69 (2015) [arXiv:1409.6190 [hep-ex]].
- [44] G. Aad *et al.* [ATLAS Collaboration], Eur. Phys. J. C **75**, no. 5, 209 (2015) [arXiv:1503.04677 [hep-ex]].
- [45] G. Aad *et al.* [ATLAS Collaboration], Phys. Lett. B **737**, 223 (2014) [arXiv:1406.4456 [hep-ex]].
- [46] R. Barbieri, A. Pomarol, R. Rattazzi and A. Strumia, Nucl. Phys. B **703**, 127 (2004) [hep-ph/0405040].
- [47] B. Fuks, M. Klasen, F. Ledroit, Q. Li and J. Morel, Nucl. Phys. B **797**, 322 (2008) [arXiv:0711.0749 [hep-ph]].
- [48] T. Jezo, M. Klasen, D. R. Lamprea, F. Lyonnet and I. Schienbein, JHEP **1412**, 092 (2014) [arXiv:1410.4692 [hep-ph]].
- [49] A. R. Zerwekh, Eur. Phys. J. C **46**, 791 (2006) [hep-ph/0512261].

- [50] A. E. C. Hernandez, C. O. Dib and A. R. Zerwekh, arXiv:1506.03631 [hep-ph].
- [51] V. Khachatryan *et al.* [CMS Collaboration], Eur. Phys. J. C **75**, no. 5, 212 (2015) [arXiv:1412.8662 [hep-ex]].
- [52] The ATLAS collaboration, ATLAS-CONF-2015-007, ATLAS-COM-CONF-2015-011.
- [53] D. M. Asner, T. Barklow, C. Calancha, K. Fujii, N. Graf, H. E. Haber, A. Ishikawa and S. Kanemura *et al.*, arXiv:1310.0763 [hep-ph].
- [54] T. Sjostrand, S. Mrenna and P. Z. Skands, Comput. Phys. Commun. **178**, 852 (2008) [arXiv:0710.3820 [hep-ph]].
- [55] R. Corke and T. Sjostrand, JHEP **1103**, 032 (2011) [arXiv:1011.1759 [hep-ph]].
- [56] J. de Favereau *et al.* [DELPHES 3 Collaboration], JHEP **1402**, 057 (2014) [arXiv:1307.6346 [hep-ex]].
- [57] M. Cacciari and G. P. Salam, Phys. Lett. B **641**, 57 (2006) [hep-ph/0512210].
- [58] M. Cacciari, G. P. Salam and G. Soyez, Eur. Phys. J. C **72**, 1896 (2012) [arXiv:1111.6097 [hep-ph]].
- [59] J. M. Butterworth, A. R. Davison, M. Rubin and G. P. Salam, Phys. Rev. Lett. **100**, 242001 (2008) [arXiv:0802.2470 [hep-ph]].
- [60] M. Cacciari, J. Rojo, G. P. Salam and G. Soyez, JHEP **0812**, 032 (2008) [arXiv:0810.1304 [hep-ph]].
- [61] A. Abdesselam, E. B. Kuutmann, U. Bitenc, G. Brooijmans, J. Butterworth, P. Bruckman de Renstrom, D. Buarque Franzosi and R. Buckingham *et al.*, Eur. Phys. J. C **71**, 1661 (2011) [arXiv:1012.5412 [hep-ph]].
- [62] A. Altheimer, A. Arce, L. Asquith, J. Backus Mayes, E. Bergeaas Kuutmann, J. Berger, D. Bjergaard and L. Bryngemark *et al.*, Eur. Phys. J. C **74**, no. 3, 2792 (2014) [arXiv:1311.2708 [hep-ex]].
- [63] Y. L. Dokshitzer, G. D. Leder, S. Moretti and B. R. Webber, JHEP **9708**, 001 (1997) [hep-ph/9707323].
- [64] M. Wobisch and T. Wengler, In \*Hamburg 1998/1999, Monte Carlo generators for HERA physics\* 270-279 [hep-ph/9907280].
- [65] M. Bahr, S. Gieseke, M. A. Gigg, D. Grellscheid, K. Hamilton, O. Latunde-Dada, S. Platzer and P. Richardson *et al.*, Eur. Phys. J. C **58**, 639 (2008) [arXiv:0803.0883 [hep-ph]].

- [66] G. Aad *et al.* [ATLAS Collaboration], Eur. Phys. J. C **74**, no. 8, 3023 (2014) [arXiv:1405.6583 [hep-ex]].
- [67] C. Englert, P. Harris, M. Spannowsky and M. Takeuchi, Phys. Rev. D **92**, no. 1, 013003 (2015) [arXiv:1503.07459 [hep-ph]].
- [68] The ATLAS collaboration, ATL-PHYS-PUB-2013-003.
- [69] T. P. Cheng, E. Eichten and L. F. Li, Phys. Rev. D **9**, 2259 (1974).
- [70] W. Grimus and L. Lavoura, Eur. Phys. J. C **39**, 219 (2005) [hep-ph/0409231].